Geophysical Journal International

Geophys. J. Int. (2024) **236,** 1785–1803
Advance Access publication 2024 January 08
GJI Seismology

https://doi.org/10.1093/gji/ggae014

An improved estimation of stress drop and its application on induced earthquakes in the Weiyuan Shale Gas Field in China

Jiewen Zhang [1,2] Hongfeng Yang [1,2,3] Jinping Zi,[1] Jinrong Su[4] and Xiaowei Chen[5,6]

[1] *Earth and Environmental Sciences Programme, The Chinese University of Hong Kong, Hong Kong S.A.R.* 000000, *China. E-mail: hyang@cuhk.edu.hk*
[2] *Shenzhen Research Institute, The Chinese University of Hong Kong, Shenzhen, Guangdong* 518057, *China*
[3] *Institute of Environment, Energy and Sustainability, The Chinese University of Hong Kong, Hong Kong S.A.R.* 000000, *China*
[4] *Sichuan Earthquake Administration, Chengdu, Sichuan* 610041, *China*
[5] *Mewbourne College of Earth and Energy Sarkeys Energy Center, University of Oklahoma, Norman, Oklahoma* 73019, *USA*
[6] *Department of Geology and Geophysics, Texas A&M University, College Station, Texas* 77843, *USA*

Accepted 2024 January 5. Received 2023 December 31; in original form 2023 July 6

SUMMARY

Stress drop is a proxy of understanding earthquake source process, and it is controversial whether the stress drops of induced earthquakes associated with hydraulic fracturing and injection activities are similar to those of tectonic earthquakes. The measurement of stress drops is usually biased due to the limitations of observation means, or hidden issues in the estimation approaches. Utilizing a local short-period seismic network, we investigate the stress drops of induced earthquakes in Weiyuan Shale Gas Field in Sichuan Province, China from 2019 to 2020. Totally 11 844 earthquakes are involved in the analysis, and their stress drops are obtained using an improved approach on the basis of the traditional spectral decomposition method combined with a global optimization algorithm to avoid stacking of spectra that is found leading to source parameter underestimation. We divide the studied area into three subareas, and the results show strong stress drop heterogeneity across the entire region. We obtain an average stress drop of 2.29 MPa, piecewise stress drop dependence to earthquake magnitude, and complex depth dependence pattern. Our results indicate that stress drops of induced earthquakes are overall consistent with the induced earthquakes in other areas as well as tectonic earthquakes in different environments. Meanwhile, the complexity in the stress drop dependence to depth possibly reflects the variability of stress drops for different earthquake triggering mechanisms.

Key words: Earthquake source observations; Induced seismicity; Seismicity and tectonics.

1 INTRODUCTION

Stress drop is a useful tool to investigate earthquakes associated with unconventional oil and gas production. It is defined as the average shear stress change accompanied by earthquake occurrence on a fault. Stress drop can be used to evaluate strong ground motion that directly relates to impacts on the environment and human society (e.g. Baltay *et al.* 2019). Besides, stress drop variability has been found relevant to fault behaviours from induced earthquakes. For instance, Wu *et al.* (2018) find that the stress drops of induced earthquake sequences in Oklahoma vary both spatially and temporally, reflecting strong fault heterogeneity potentially related to fluid injection. However, stress drop estimation is usually subject to uncertainties from various sources. Similar approaches using different data sets with different observatory setups sometimes lead to inconsistent absolute values (e.g. Allmann & Shearer 2007 compared to Zhang *et al.* 2022 for Parkfield area microearthquakes), and the application of different methods on the same study area or similar tectonic environments often results in inconsistent conclusions such as whether earthquakes are self-similar (e.g. Mayeda *et al.* 2005; Oye *et al.* 2005; Shearer *et al.* 2006; Allmann & Shearer 2009; Oth 2013; Uchide *et al.* 2014; Goebel *et al.* 2015; Zhang *et al.* 2022). Therefore, mitigating the uncertainties in the stress drops is highly important to achieve less biased interpretations.

There are open debates about whether the source characteristics of induced earthquakes are similar to that of natural earthquakes. One of the hot topics focuses on whether the stress drops of induced earthquakes are similar to those of natural earthquakes in terms of their absolute values and dependence on earthquake scales. Huang *et al.* (2017) investigated the stress drops of both types of earthquakes in multiple research areas, concluding that there is no systematic difference between them. This was supported by other studies (e.g. Wu *et al.* 2018; Holmgren *et al.* 2019 and Chu & Sheng 2023), who found similar stress drop level to natural earthquakes and self-similar relationship of induced earthquakes in Oklahoma, USA, Western Canada and Sichuan, China. On the other hand, studies

such as Agurto-Detzel *et al.* (2017) found lower absolute stress drops of <1 MPa of induced earthquakes in southeastern Brazil, and Klinger & Werner (2022) reported non-self-similarity of induced earthquakes. Goertz-Allmann *et al.* (2011) observed varied stress drop levels with location, indicating that the stress drops of induced earthquakes near injection are lower than farther ones, and such pattern is consistent with earthquake migration accompanied by fluid migration. The differences in the results may have multiple sources, including the mechanisms of the induced earthquakes, different ways of data processing, and the differences and limitations of various methods.

Rongxian–Weiyuan area, located in Southeastern Sichuan Province in China, is a suitable candidate to explore the problem mentioned above due to the high seismicity in the recent years from injection activities. The area was seismically silent in the history until massive shale gas exploration started since 2014 (Yang *et al.* 2020). A drastic increase in seismicity appeared in 2018 coinciding with intensive fracking activities, which was followed by multiple $M_L > 3$ and even a few $M_L > 4$ earthquakes, including a damaging and deadly M_L 5.2 earthquake in Rongxian County in late February 2019 after the Chinese Spring Festival. The earthquake is thought to occur on Molin Fault, which is a thrust fault (the dominant focal mechanism for $M_s > 3$ earthquakes in the region, Yi *et al.* 2020) with NW–SE orientation located on the south of Weiyuan anticline, the characteristic geological structure in the region. There are concurrent hydraulic fracturing activities in a nearby injection well; whether the major earthquake was triggered by fluid is still unclear, as there is no strong evidence of fluid migration from injection zones to the east of the fault (Yang *et al.* 2020). Stress drop can be a potential candidate that may help understand the earthquake triggering mechanisms in the subsurface (e.g. Goertz-Allmann *et al.* 2011; Huang *et al.* 2017; Chu & Sheng (2023) obtained the stress drops of 17 M 2.2–2.75 earthquakes to be ranging from 2.5 to 54.7 MPa, but large-scale stress drop analysis that characterizes the tectonic heterogeneity similar to Allmann & Shearer (2009) and Zhang *et al.* (2022) in this region is yet missing.

Stress drops of low-to-intermediate scaled earthquakes are usually estimated using seismic waves rather than geological or geodetic approaches, as these earthquakes are not capable of creating visible surface displacements. A common method is a spectral ratio method calculating the ratio between the observed spectrum of an earthquake and that of a nearby smaller earthquake as an empirical Green's function (eGF; e.g. Abercrombie 2014; Lengliné *et al.* 2014; Huang *et al.* 2017; Shearer *et al.* 2019; Chu & Sheng 2023). Such approach requires careful selection of eGF events to be associated with the main event, which are usually 1–2 magnitude larger than the eGF events (Abercrombie *et al.* 2021). Thus, this method can hardly solve for the stress drops for already small earthquakes (e.g. $M < 2.0$), and cannot be applied to stress drop analysis on a large data set including several 10 000s of earthquakes due to low efficiency of eGF selection and source parameter inversion. The spectral decomposition and stacking method (Shearer *et al.* 2006) is developed to solve for the stress drops in seismically dense areas. This method iteratively separates the average source term, station term and path information for each earthquake–station pair, thus it requires large-scale data feed. It has been applied to numerous studies on stress drop analysis covering the scales from locally to globally (e.g. Allmann & Shearer 2007; Allmann & Shearer 2009; Chen & Shearer 2013; Uchide *et al.* 2014; Chen & Abercrombie 2020; Pennington *et al.* 2021; Zhang *et al.* 2022). However, it requires a strong assumption of earthquakes self-similarity meaning all the earthquakes should have similar stress drop levels, which is still under debate as mentioned above. Then improved methods are developed to avoid such assumption, such as Trugman & Shearer (2017) obtained an optimized linearly scaling relationship of log10 stress drops to the earthquake magnitude, and Chen & Abercrombie (2020) avoided the assumption of stress drop dependence on earthquake magnitude; the former found earthquake non-self-similarity for small earthquakes (e.g. $M < 2$). Zhang *et al.* (2022) use larger earthquakes ($M > 3$) to correct for the potential underestimation of small-earthquake stress drops following the approach by Chen & Abercrombie (2020), and also found obvious magnitude dependence at low magnitudes. Whether the non-self-similarity originates from the methods remains unclear, though it has been found that the limitation of sampling rate could result in underestimated corner frequencies (Chen & Abercrombie 2020; Zhang *et al.* 2022). Another possible source of stress drop biases could lie in the manner the spectra are processed in various methods—stacking. The purpose of stacking the spectra is to mitigate the influence from noise, but stacking the spectra across earthquakes could potentially oversmooth the fall-off point of the spectra introducing larger uncertainties in the earthquake corner frequencies.

In this study, we aim at designing a new approach inheriting the spectral decomposition method, while attempting to solve the problem of unexpected self-similarity assumptions and testify if stacking could lead to biased stress drop estimation. We will perform a series of synthetic tests to evaluate the performance of the proposed method against a previous method applied in Chen & Abercrombie (2020). After that, the proposed approach will be implemented to estimate stress drops of the large-scale induced earthquakes in Sichuan, China, and the stress drops will be used to investigate the earthquake scaling relationship, as well as the characteristics of the stress drops in the region.

2 METHOD

2.1 Spectral-decomposition-based approach

An observed spectrum of an earthquake on a seismometer can been seen as the convolution of an event term (source), a path term and a site term. Estimating the source parameters relies on the source information, therefore it is important to separate the source contribution from other effects in the observed spectra, such as site information and travel path effect, which are usually unknown and hard to directly remove. The spectral-decomposition method solves for the site and path information and isolate the source spectrum in an iterative way, and the source spectrum does not reflect any directivity impacts because it is the averaged spectra recorded at the stations over all azimuths. (Shearer *et al.* 2006; Allmann & Shearer 2007; Zhang *et al.* 2022) (Fig. 1). We follow Shearer *et al.* (2006) to obtain a separated average event term for each earthquake from the observed spectra.

However, it should be noted that the event term is not equal to its source term; it reflects the relative shape of a source term, and extra correction is required on the event spectra including residual site amplification and path effects. Besides, the proposed method assumes a simple homogeneous attenuation model, and the path term is only related to travel time; thus, the correction could majorly contain the compensation to the attenuation information. To obtain the correction, different approaches assume either a reference site term (Bindi *et al.* 2020a; Oth *et al.* 2011) or a source model (Shearer *et al.* 2006; Trugman & Shearer 2017; Shearer *et al.* 2019; Chen & Abercrombie 2020; Zhang *et al.* 2022). This study

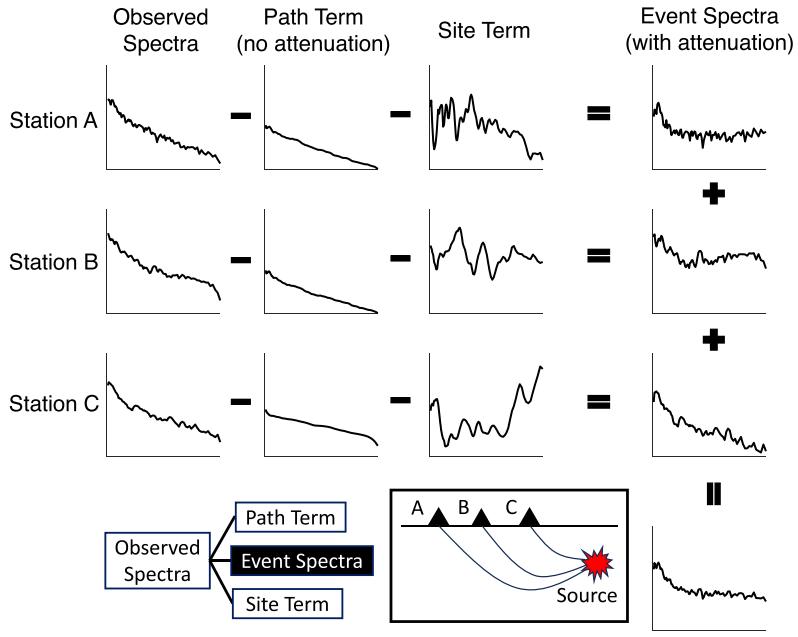

Figure 1. Demonstration of the spectral decomposition (SD) method extracting the event spectra from observed spectra at stations. The figure shows an example of one earthquake, but the SD method is applied on a large data set. The example spectra are shown in log10 scale on *x*-axis (frequency) and linear scale on *y*-axis (amplitude).

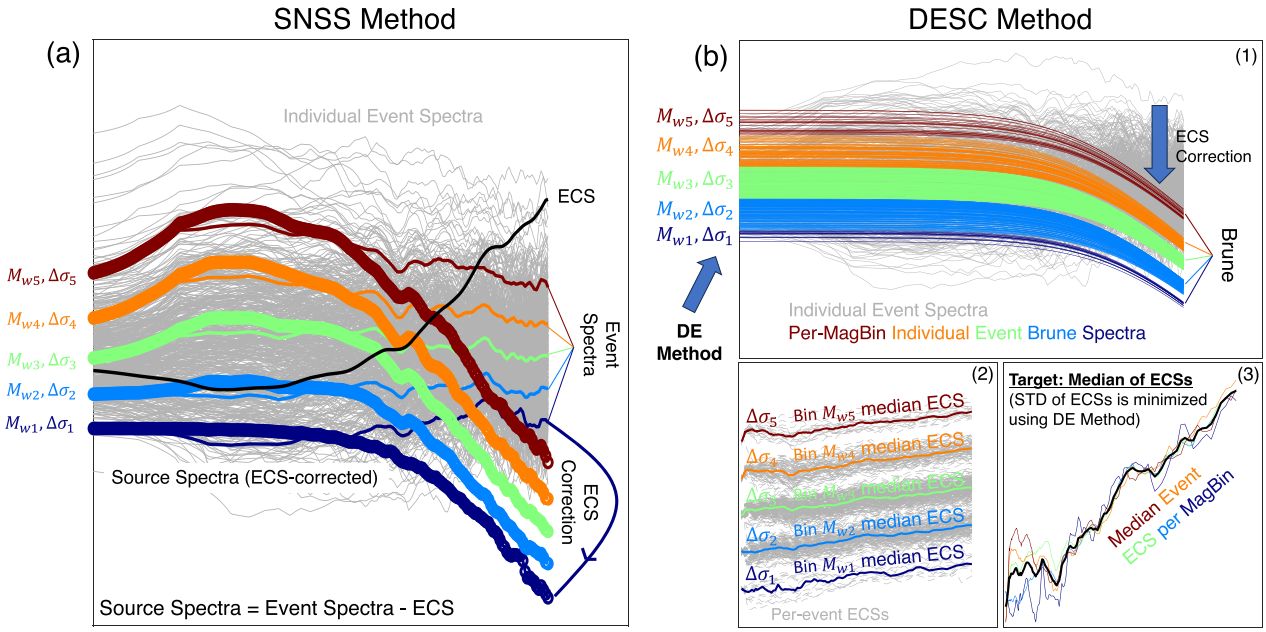

Figure 2. (a) Demonstration of the workflow of obtaining the empirical correction spectrum (ECS) using the SNSS (previous) method with the event spectra obtained using the spectral decomposition (SD) method. Different colours of thin curves represent the stacked event spectra that are sorted into different magnitude bins from M_{w1} to M_{w5}. The bold curves represent the ECS corrected spectra (black curve) from the thin curves in the corresponding magnitude bins. The ECS curve is obtained by fitting the bold curve in magnitude bin M_{w1} (the lowest magnitude bin) to the Brune's model calculated using the moment and stress drop in this bin. (b) Demonstration of the workflow of obtaining the ECS using the DESC (new) method. 1: Assume stress drops in the five magnitude bins, obtain Brune's spectra for each earthquake (coloured curves), and the ECSs for the individual earthquakes are their difference from the corresponding event spectra (grey curves). 2: Calculate the medians of the ECSs of individual earthquakes (grey curves) in their own magnitude bins (coloured bold curves). 3: Minimize the difference among the median ECSs in different magnitude bins (coloured thin curves) utilizing the DE method, and finalize an overall ECS for further spectral analysis (bold black curve) by calculating the median of the per-magnitude-bin median ECSs. Note that the *x*-axis scales in 2 and 3 are set to linear to show the linearity of the ECSs against frequency in this method.

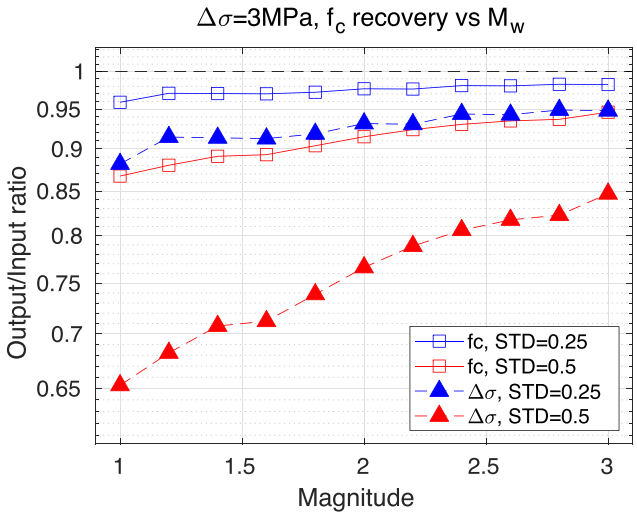

Figure 3. Corner frequency recovery ratio after stacking the Brune-shape theoretical spectra at different magnitudes. Magnitude bins are set to 1.0–3.0 with an interval of 0.2; in each magnitude bin, 200 earthquakes with the same magnitude (centre of each bin) obtain their synthetic spectra by assigning them with normally distributed stress drops, centred at a reference stress drop of 3 MPa with a standard deviation (STD) of log10 stress drop of 0.25 (blue curve) and 0.5 (red curve), to simulate realistic stress drop scattering. The stacked spectrum in each magnitude bin is compared to the Brune's model to estimate an inverted corner frequency, and the recovery ratio (the square markers) is defined as the ratio between this inverted corner frequency and the theoretical Brune's spectrum at the corresponding magnitude and 3 MPa stress drop (aka. reference spectrum). The triangle markers denote the stress drop recovery ratio in each magnitude bin.

follows the latter, and the correction term accounting for attenuation information is named the empirical correction spectrum (ECS). Since the ECS represents a homogeneous attenuation distribution over the space spanned by the involving earthquakes and stations, for heterogeneous underground medium the proposed ECS may result in biased source spectrum for an earthquake after correction (as demonstrated by Allmann & Shearer 2007; Zhang *et al.* 2022). The complex structure from body-wave tomography (Zi *et al.* 2023) and ambient noise imaging (Zeng *et al.* 2020) of the Weiyuan area may indicate heterogeneity of attenuation, therefore an appropriate data processing workflow is needed to mitigate such influence on the stress drop estimation, which will be introduced in Section 4. Then, the source spectra representing the real earthquake source information can be obtained by subtracting the ECS from the event spectra.

2.2 Calculation of stress drop from earthquake source spectra

We implement Brune's source spectrum model to estimate the earthquake stress drops for small earthquakes (Brune 1970). In this model, the far-field displacement spectrum of an earthquake can be represented as:

$$s(f) = \frac{M_0}{1 + \left(\frac{f}{f_c}\right)^n}, \tag{1}$$

where M_0 is the seismic moment of the earthquake, f_c is the corner frequency describing the source duration and n is the fall-off rate (n is set to 2 in this study representing an ω^{-2} model). By assuming a simple circular rupture for a small earthquake, the corner frequency can be written as (Brune 1970; Madariaga 1976):

$$f_c = k\frac{\beta}{r}, \tag{2}$$

where β represents shear wave velocity, k is a constant depending on model assumptions (e.g. Kaneko & Shearer 2014, 2015), and r stands for source radius. We choose $k = 0.32$ based on Madariaga (1976), consistent with Allmann & Shearer (2007) and Kaneko & Shearer (2015). For the shear velocity, we use the tomography results of the same studied area from Zi (2022), and for each earthquake, the shear velocity is determined at the nearest grid point value in the tomography results to the earthquake location. Then the stress drop ($\Delta\sigma$) can be calculated from seismic moment and source radius according to Eshelby (1957):

$$\Delta\sigma = \frac{7}{16}\left(\frac{M_0}{r^3}\right) = M_0\left(\frac{f_c}{0.42\beta}\right)^3, \quad f_c = 0.32\frac{\beta}{r}. \tag{3}$$

This relationship enables derivation of stress drop from corner frequency for a single earthquake. It should be noted that the stress drop estimated from spectral fitting must be considered an approximation, because it is related to the dynamic properties of the earthquake based on a simple circular rupture model assumption (Brune 1970; Madariaga 1976), which essentially differ from the static stress drop that is derived from the actual slip and rupture dimension.

2.3 Empirical correction spectrum (ECS) estimation

As discussed in Section 2.1, an ECS is required for an earthquake to extract its source term from the event term separated from earthquake–station-pair spectra. Current studies use different constraints on the source model assumptions: all of the methods sort the event spectra of earthquakes into small-size moment magnitude bins (usually the size is set to 0.2–0.3), and stack the event spectra in each magnitude bin and obtain a representative average event spectrum for each bin. Then, average stress drops in these magnitude bins are needed to obtain an overall ECS; Shearer *et al.* (2006) and Trugman & Shearer (2017) require fixed stress drop scaling relationship with earthquake moment (constant stress drop, or first-order scaling stress drop across all the magnitude bins), while Chen & Abercrombie (2020) and Zhang *et al.* (2022) avoid assuming the scaling relationship and solve for an ECS by minimizing the difference between ECS-corrected source spectra and Brune's spectra in different magnitude bins (Stacking with No Self-Similarity assumption, SNSS, see demonstration in Fig. 2a). Both constraints have their own advantages and disadvantages: constraining the scaling relationship has lower time complexity as it does not rely on massive spectral fitting by magnitude bin, while constraining the spectral shape cannot avoid this; on the other hand, fixing the scaling relationship may risk obtaining a significantly different attenuation level than reality (Shearer *et al.* 2006) or a complex trade-off between the attenuation (ECS) and the scaling factor of stress drop against magnitude (Trugman & Shearer 2017; Shearer *et al.* 2022). The key to alleviating the trade-off between calculation efficiency and accuracy of ECS is to accelerate the per-bin average stress drop estimation while keeping stress drops free from any assumed scaling.

Another hidden issue in the current methods is that after the earthquakes are sorted into different moment magnitude bins, stacking the log10 spectra in the same magnitude bin is required to obtain the average moment and stress drop, which could cause biased spectra and underestimated corner frequency (this will be further

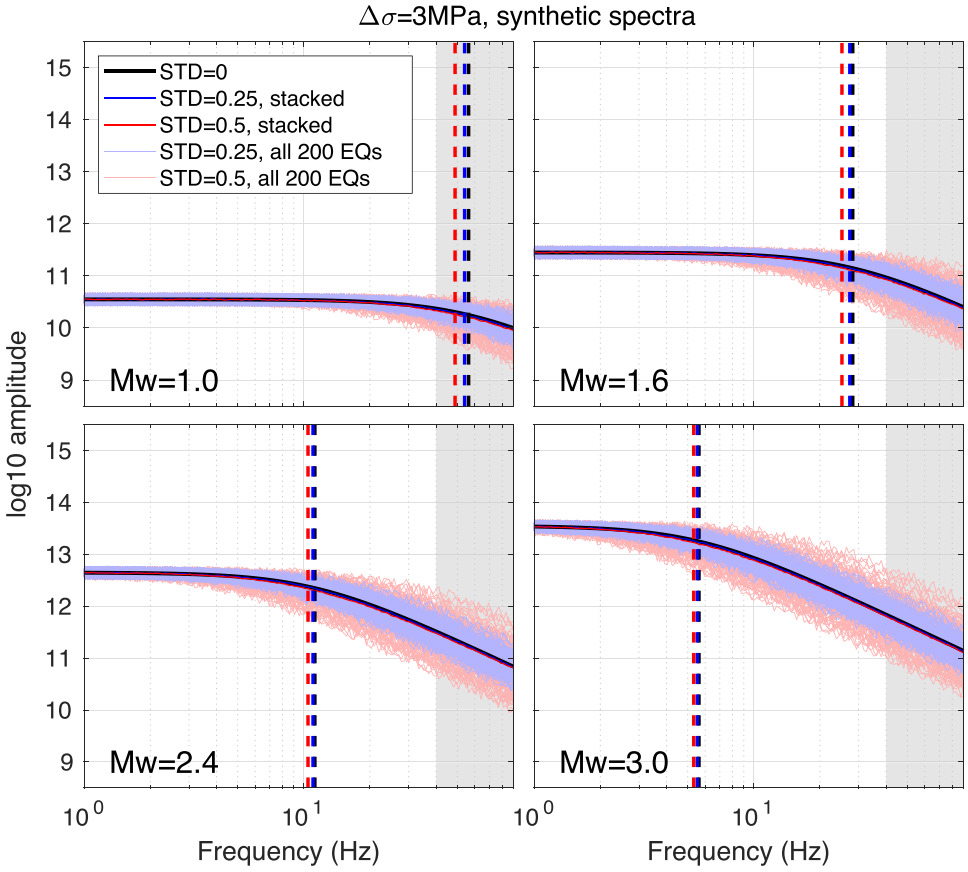

Figure 4. Visualization of the extent of corner frequency underestimation at different magnitudes (M_w 1.0, M_w 1.6, M_w 2.4 and M_w 3.0) in Fig. 2. The black, blue and red curves represent the reference spectrum, stacked spectrum at STD = 0.25, and stacked spectrum at STD = 0.5. The shallow blue and red curves are the individual theoretical Brune-shape spectra corresponding to each STD level. The vertical dashed lines denote the position of the inverted corner frequencies and the reference corner frequency with matching colours. The grey area marks the frequency range higher than the upper limit 40 Hz used for corner frequency inversion.

explained in Section 3). To solve the problems above, we design a new approach to solve for the ECS from the event spectra called the differential-evolution-based spectral correction (DESC). It implements a global-optimization algorithm named differential evolution (DE) developed by Storn & Price (1997) to find the optimized combination of stress drops in all the magnitude bins, which is a high-dimensional inversion problem. The DE algorithm has been applied in earth science studies for different purposes, for example earthquake hypocentral location (Gharti *et al.* 2010) and 1-D underground velocity structure inversion (Zhang *et al.* 2016). The proposed method is capable of providing fast and accurate solution of average stress drops using the individual event spectra from the data set.

The workflow of the DESC method is below (see demonstration in Fig. 2b):

Step 1: Sort the event spectra into different moment magnitude bins.
Step 2: Randomly generate a set of average stress drops for the magnitude bins, and for each magnitude bin, calculate an individual ECS for each earthquake from the difference between its event spectrum and the Brune spectrum calculated using its own moment and the stress drop in its belonging magnitude bin, and obtain an overall ECS by calculating *the median of the individual ECSs* in each magnitude bin at each frequency sampling point.
Step 3: Compare the overall ECSs in different bins by calculating their per-frequency-sample standard deviation as the objective function.
Step 4: Apply the DE method to iteratively minimize the objective function in Step 3 to find an optimized set of stress drops in Step 2, and the optimized set corresponds to a final optimized ECS (the median of all the optimized per-bin overall ECSs). The minimization of the objective function here is on the basis that the attenuation variability in a reasonably small area should be ignorable, and the ECSs for all the earthquakes in this area should be highly similar.

In Step 4, we obtain an ECS that can correct for the source spectra of individual earthquakes. Then, an identical spectral fitting approach to that in Chen & Abercrombie (2020) is performed to compare each source spectrum to Brune's model by each frequency sample, and solve for the stress drop of each earthquake. It is important to clarify that we assume a constant Q for the attenuation model, and in Step 2, the reason that the individual ECSs obtained from event spectra in a single bin can be stacked is that with a frequency-independent Q-value, the ECS curve is expected to be linear against frequency with a slope proportional to the average t^* in the area; oppositely, in the current methods the stacking approach may introduce biases because the event spectra, supposedly the combination of local attenuation information and the source spectra, is non-linear against frequency and should not be stacked directly in mathematical sense.

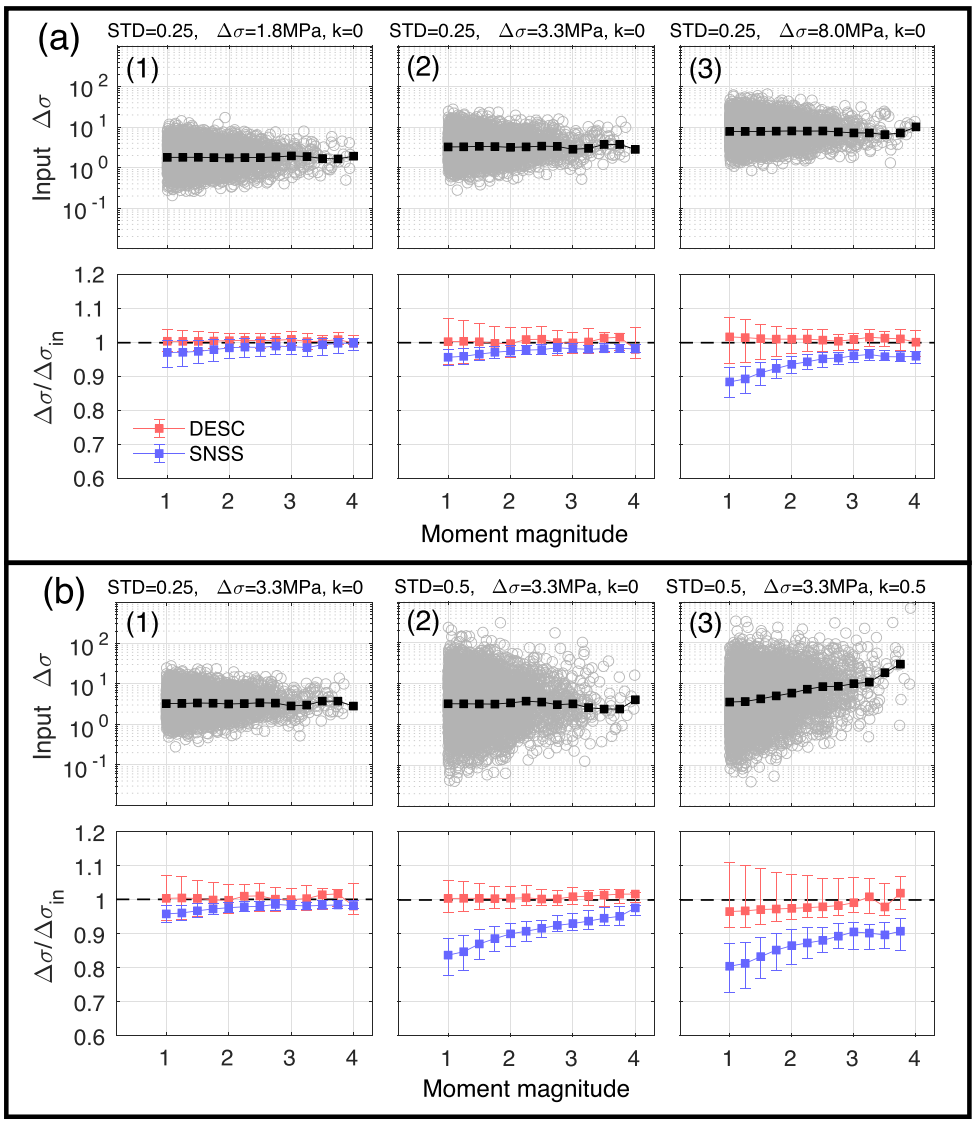

Figure 5. Stress drop recovery ratio applying the SNSS (blue curve) and DESC (red curve) method. (a) tests using different input stress drops: 1.8 MPa (1), 3.3 MPa (2) and 8.0 MPa (3), the same log10 input stress drop STD, and the same input stress drop scaling with magnitude; (b) tests using the same input stress drop of 3.3 MPa, different log10 stress drop STD of 0.25 and 0.5, and the same input stress drop scaling with magnitude (1 versus 2); the same input stress drop of 3.3 MPa, the same log10 stress drop STD of 0.5, and different input stress drop scaling factor 0 and 0.5 (2 versus 3). In each subplot, the upper panels represent the input stress drops VS. magnitude with black squares denoting the median stress drops in the magnitude bins of 1.0–4.0 sized 0.5, and the lower panels represent the stress drop recovery ratios using the two methods, accompanied by median values as squares and error bars pointing out the 25th and 75th percentile in different magnitude bins.

2.4 Stress drop correction with depth-dependent shear velocity

Stress drop estimates are sensitive to vertical shear velocity change as shown in eq. (3). Essentially, the corner frequency is a representation of the rupture duration, thus related to rupture velocity that usually is assumed proportional to depth-dependent shear wave velocity in source parameter analyses (Allmann & Shearer 2007; Kaneko & Shearer 2014; Uchide *et al.* 2014; Abercrombie *et al.* 2021; Zhang *et al.* 2022), while some others set the rupture velocity as a constant of 0.9 times of the average local shear velocity (Shearer *et al.* 2006; Lengline *et al.* 2014). It has been found that using a depth-dependent rupture velocity model reduces the trend of depth dependence (Allmann & Shearer 2007; Zhang *et al.* 2022). In Abercrombie *et al.* (2021), they systematically discussed earthquake focal depth as a factor of impact on stress drop estimation, revealing that applying a depth-dependent rupture velocity model and accounting for the attenuation over depth, as mentioned above, leave only negligible depth dependence of stress drops. In this analysis, we also implement such a rupture velocity model based on the tomography results by Zi *et al.* (2023).

3 SYNTHETIC TESTS

We perform a series of tests using synthetic earthquake moments and Brune-shaped spectra to evaluate the performance and compare the difference between the DESC and SNSS methods.

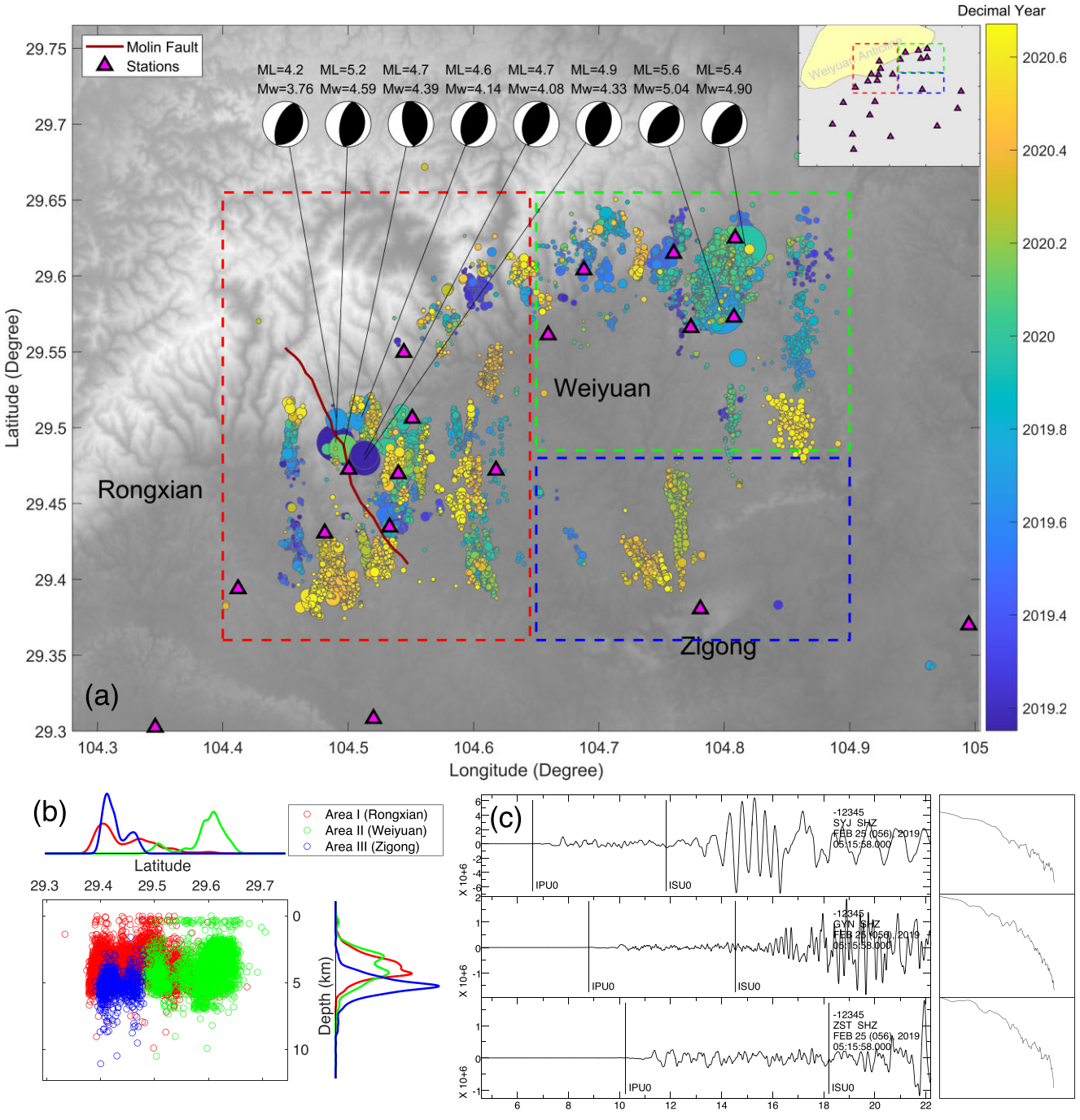

Figure 6. The statistics of the seismicity in the studied area. (a) Seismicity map. The circles indicating the individual earthquake locations are coloured by their occurrence time and sized by their local magnitudes. The magenta triangles represent the short-period local seismic stations utilized in this study. The beach balls show the focal mechanisms of the local magnitude larger than 4 earthquakes in the area. The brown curve depicts the surface trace of Molin fault. Three dashed rectangles in red, green, and blue show the three studied subareas. In the embedded panel, the shallow yellow block roughly circles the location of the Weiyuan anticline. (b) Location statistics over latitude and depth. The histograms indicate the percentage of earthquakes at a certain latitude or depth. Colours are matched with the rectangles in (a). (c) The left-hand panel shows the example vertical-component waveforms of the February 2019 M_L 4.9 earthquake in Rongxian recorded by station SYJ, GYN and ZST. The right-hand panel shows the corresponding event spectra of the waveforms in their own rows calculated by a multitaper based method named 'pmtm' in MATLAB.

First, we try to reveal the potential influence of stacking spectra on source parameter estimation (such as corner frequency and stress drop), in light of which we then implement the DESC and SNSS methods on the synthetic data set with input source parameters to compare both methods in terms of the ability to recover the input. Finally, we demonstrate the time complexity of the DESC against the SNSS method by performing repetitive runs.

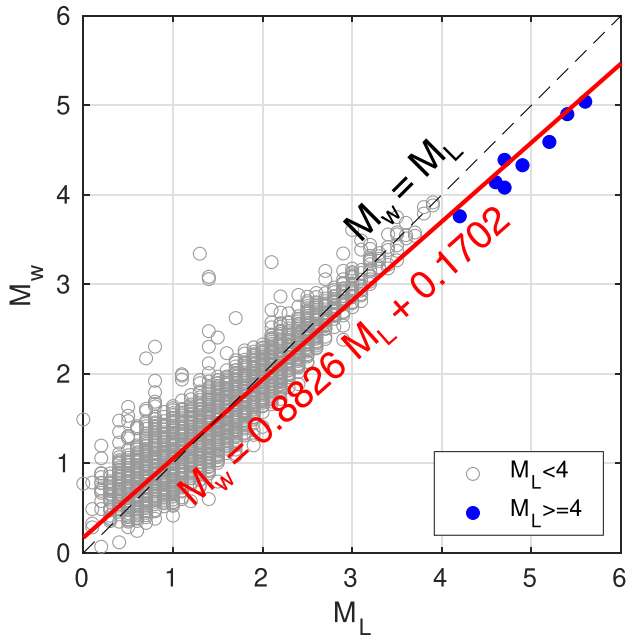

Figure 7. The magnitude calibration process. The thick red line shows the linear regression of the moment magnitudes and the local magnitudes of all the earthquakes. The thin dashed black line shows where the moment magnitude is equal to the local magnitude. The grey open circles and the blue closed circles represent the earthquakes with local magnitudes lower and higher than 4. The two magnitude scales are assumed equal at $M_w = M_L = 3.0$ in the magnitude calibration process.

3.1 Source parameters from stacked spectrum versus input Brune's spectrum

Stacking of spectra is widely used in different methods to mitigate the influence from noisy spectra on source parameter estimation; however, this could lead to biased estimates provided limited frequency band. To visualize this, we design a test to compare the source parameter results with and without stacking of spectra. We choose 11 magnitude bins ranging from commonly seen M_w 1.0 to M_w 3.0 with an interval of M_w 0.2 to investigate the influence on different scales of earthquakes. In each magnitude bin, there is a reference Brune's spectrum with 3 MPa stress drop, and we generate 200 Brune-shape spectra corresponding to 200 earthquakes with normally distributed log10 stress drops centred at 3 MPa and the same moment magnitude, and these spectra will be stacked within each magnitude bin and fitted to Brune's shape. White noise is added to the Brune's spectra, which is set to perturbate the log10 Brune spectra by random numbers generated between −0.25 and 0.25. We also investigate whether the scattering of the stress drops affect the stacking results by setting two standard deviations of normally distributed log10 stress drops (STD): 0.25 and 0.5 according to the estimates in Zhang *et al.* (2022). The stacked spectra in different magnitude bins are fitted to Brune's shape to estimate their corner frequencies within the frequency band of 1–40 Hz, and the estimated corner frequency of the stacked spectrum in a certain bin is compared to the 200 input individual corner frequencies in this bin.

Compared to the input reference Brune-shaped spectrum, we calculate the recovery ratio as the output source parameters divided by the input (Fig. 3). It can be observed that the corner frequency is underestimated at all the magnitudes, as well for the stress drops which is upscaled cubically from the corner frequencies; the underestimation is more significant for smaller magnitudes than larger magnitudes, which forms artificial magnitude scaling of source parameters. As for different scattering levels of individual input stress drops (different STDs), in M_w 1.0 bin the STD = 0.5 case produces 34 per cent of underestimation compared to 12 per cent from the STD = 0.25 case, while in M_w 3.0 bin such comparison becomes 15 per cent versus 5 per cent. Such difference in the scaling from two different scattering levels indicate that the stacking methods on highly scattered stress drop values would lead to artificial magnitude scaling, and in real data cases the apparent non-self-similarity conclusions.

We also showcase the corner frequency recovery in four reference magnitude bins of M_w 1.0, M_w 1.6, M_w 2.4 and M_w 3.0 (Fig. 4). It can be found that the corner frequencies estimated in the M_w 1.0 bin have exceeded the fitting upper bound of 40 Hz, meanwhile in the M_w 1.6 bin the corner frequencies are around 60–70 per cent of the upper bound. This finding matches the discussion in Chen & Abercrombie (2020) that only the corner frequencies below 25 per cent of the upper bound can be resolved with high confidence, but this does not explain why the corner frequencies are still underestimated in M_w 2.4 and M_w 3.0 bins, albeit smaller. We suggest that the root of the underestimation is the distorted spectral shape after stacking the Brune-shaped spectra, shown as the difference between the black and red curves in Fig. 4 sharing the same plateau a.k.a. seismic moment. With that said, the biased stress drop estimates could also be ascribed to the frequency band limitation—we need a wide frequency band to ignore the distortion of the stacked spectrum near its fall-off spot after stacking.

Here we reveal that the application of stacking on similar-magnitude earthquake spectra will result in absolute stress drop underestimation, and its artificial magnitude scaling simultaneously. Both could contribute to biasing the interpretations related to stress drops. Next, we visualize how the DESC method mitigates this issue.

3.2 Stress drop recovery, DESC versus SNSS

As discussed above, the DESC method does not involve direct stacking of spectra, thus we compare its ability to preserve the true source parameters with the SNSS method. We randomly generate 500 earthquakes as a subset, which holds a moment magnitude range of M_w 1.0 to M_w 4.0, and their input stress drops are normally distributed with Brune-shaped spectra. We also add noise perturbation to the spectra; however, to better simulate realistic situations we introduce natural noise extracted from our Weiyuan earthquake waveform data set, and the signal-to-noise ratios (SNR) of individual synthetic earthquakes range from 1.5 to larger than 10 000 within 1–40 Hz. Here we perform a more comprehensive investigation on multiple factors that may cast influence on the performance of source parameter recovery when solving for individual earthquake stress drops: absolute stress drop level, stress drop scattering, and whether there is originally magnitude scaling of stress drops. Both methods are applied to solve for the individual stress drops and we calculate the stress drop recovery ratio of each earthquake; the process is repeated 10 times to mitigate uncertainties in the estimates. The frequency band for spectral fitting is 1–40 Hz, and the magnitude bin size for the two methods is set as 0.2.

We first set three different average stress drops as the reference of the normal distribution, and test the 500 earthquakes on them respectively: 1.8, 3.3 and 8 MPa simulating low, intermediate and

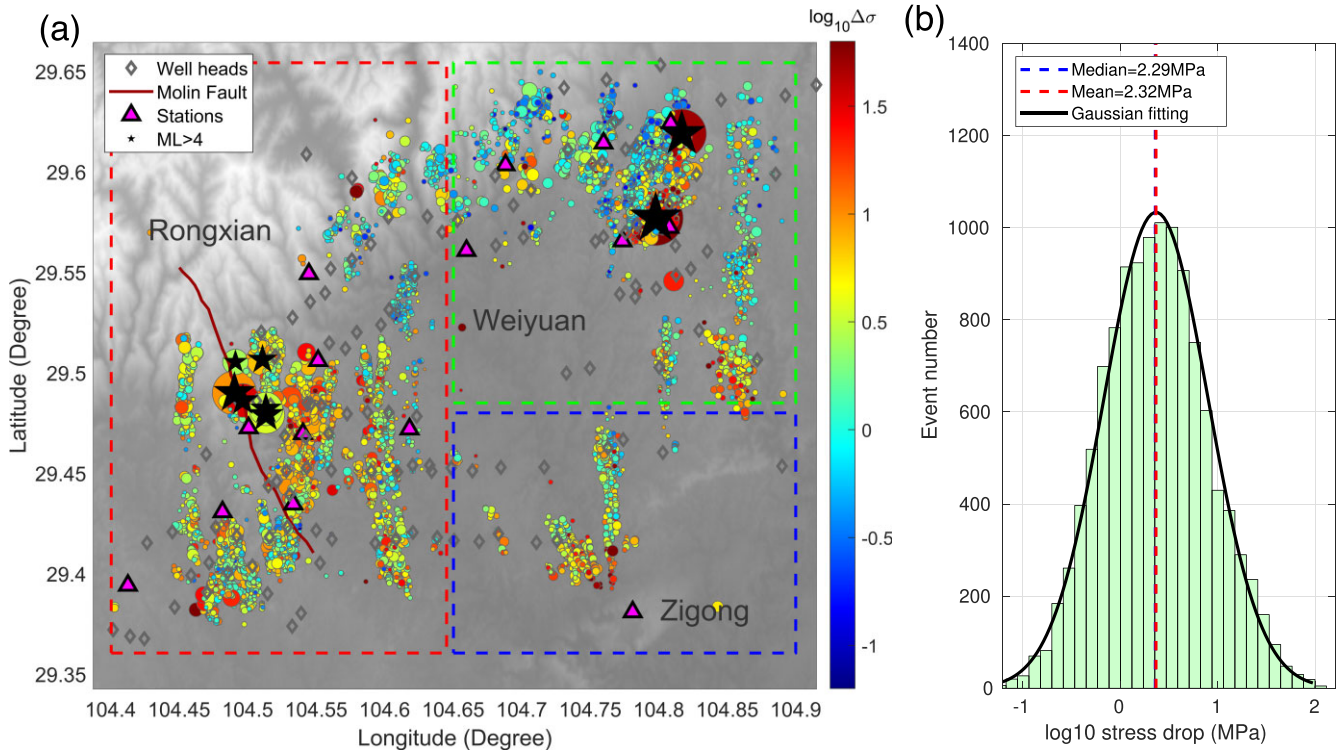

Figure 8. (a) Stress drop distribution over space in the studied area. Circle colours indicate the log10 stress drop values, and circle sizes the local magnitude. Black stars emphasize the locations of the $M_L > 4$ earthquakes. Diamonds show the locations of the local operation well locations. Other markers are identical to those in Fig. 6(a). (b) A histogram of log10 stress drops over the whole studied area. The blue and red dashed lines show the median and average log10 stress drops, respectively. The black curve is the Gaussian fitting of the histogram.

high stress drops in reality. We set the input stress drop standard deviation (STD) as 0.25 in log10 scale, and not scaled with magnitude (Figs 5a and S2). It is found that when the input average stress drop is 1.8 and 3.3 MPa, the SNSS method results in a maximum stress drop underestimation of 3 per cent for M_w 1, and nearly no underestimation for M_w 4; for a larger input average stress drop at 8 MPa, the underestimation increases to ∼10 per cent for M_w 1 and 5 per cent for M_w 4. As a comparison, the DESC method almost preserve the input values for 1.8, 3.3 and 8 MPa input, though a slight overestimation of ∼1 per cent due to the presence of noise in the spectra in the case with 8 MPa input. For all three input values, when the SNSS method is applied we obtain slight artificial magnitude dependence of stress drops, while there is no obvious scaling present from the DESC method.

Similar to the test in Section 3.1, we increase the log10 stress drop STD from 0.25 to 0.5 so the stacked spectra will be further biased, see Fig. 5b (1, 2) and Fig. S2. the STD here is a reference based on the stress drop measurements in Zhang *et al.* (2022), and in some other studies the STD can be larger (e.g. Shearer *et al.* 2006; Allmann & Shearer 2007). In the SNSS results, we observe obviously enlarged underestimation for all three input average stress drops. For the 1.8, 3.3 and 8 MPa cases, the underestimation becomes 13, 16 and 25 per cent for M_{w1}, respectively. Even the largest earthquakes at M_w 4 also suffer from more underestimation up to 10 per cent like in the 3.3 and 8 MPa cases. The underestimation increases as the average input stress drop increases, as a larger stress drop means that smaller earthquakes will have higher corner frequencies approaching or exceeding the upper limit for spectral fitting. However, similar to the STD = 0.25 case, the DESC method is still capable of recovering the input stress drops.

Lastly, considering the debates on earthquake self-similarity, we set up the stress drops not only based on normal distribution, but also on different input scaling relationship (scaling and non-scaling) to simulate two possible interpretations on earthquake self-similarity, see Fig. 5b (2, 3) and Fig. S2. All the parameters are inherited from the two test sets above. For the SNSS method, applying an input scaling relationship only result in minimal increase in the stress drop underestimation at all moment magnitudes, which is incomparable to that by increasing the STD. On the contrary, the recovery ability of the DESC method is still not visibly affected by this.

In a series of tests above, we observe that the DESC method can nearly recover the input stress drops, while the SNSS method always produce both underestimation and artificial scaling. The test result is consistent with the results in Section 3.1 in terms of the influence on stacking, and further proves that the proposed DESC method can avoid the source parameter underestimation and artificial magnitude scaling problems in a synthetic environment. However, it is still important to note that the DESC method suffers from relatively higher uncertainties; stacking can naturally suppress the noise in the spectra, while in DESC the noise is less smoothed. The mathematics relevant to the synthetic tests above is demonstrated in the Appendix for the readers' convenience.

3.4 Algorithm time complexity, DESC versus SNSS

To demonstrate the performance of the DESC method, in Fig. S1 we compare its time complexity with the SNSS method. In the test data set, we include 500 earthquakes in a spatially compact region, which should provide stable ECS solution according to a test by

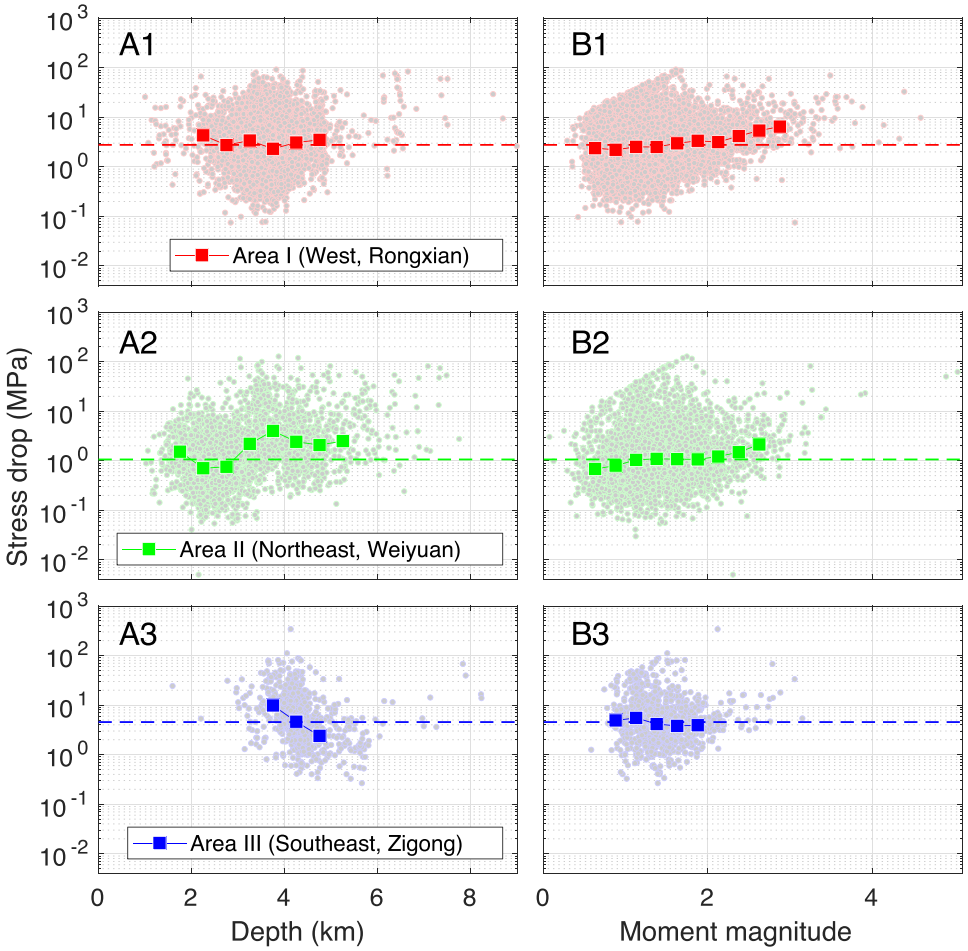

Figure 9. Stress drop statistics in the three subareas with colours matching the rectangles in Fig. 5(a). (a, b) stress drop dependence on depth and magnitude, respectively. (1–3) The stress drop in the three subareas. In each panel, the dots represent the individual stress drop values, and the squares with the corresponding colours represent the median values in magnitude bins with an interval of 0.5, and depth bins with an interval of 0.5 km. It is required that in each bin there are at least 50 data points. The horizontal dashed lines indicate the median stress drop levels in these cases.

Zhang *et al.* (2022). The DESC method returns the optimized ECS much faster than the SNSS method by 37.5 per cent on average after a full run of 500 iterations. Additionally, we test the stability of the DE algorithm on the stress drop set convergence. After five repetitive trials, the randomly generated initial stress drops all converge to the same values after around 260 times of iteration. If the test stopped at the convergence point, the runtime of the DESC would be 62.5 per cent on average faster than the SNSS. The test above shows that the DESC is capable of solving for the ECS both efficiently and accurately. However, the computational cost could rise rapidly if the maximum iteration time or random stress drop sets per iteration is not appropriately designed, or the number of earthquakes participating the iteration process is too large. Here using 500 earthquakes is a reasonable trial.

4 DATA AND RESULTS

Next we shall apply our new methods to derive stress drops of earthquakes in the Weiyuan shale gas field, Sichuan, China. The shale gas reservoir in Rongxian–Weiyuan area is covered by the upper Ordovician Wufeng Formation to lower Silurian Longmaxi Shale Formation at depths of 1.5–4.5 km (Wu *et al.* 2019). The Wufeng–Longmaxi formation has an average thickness of 35–40 m, which is a good target for shale gas productivity. The shale depths vary from the northwestern to the southeastern, with gradual increment approximately from 2 to 4 km (Ma *et al.* 2020). Three major production zones, Zi-201, Wei-202 and Wei-204, include multiple operation wells aligned with shale depth contours and Weiyuan anticline trace, and they are thought to be mostly under active operation in the studied time range according to the increasing seismicity.

In the stress drop analysis, we include a total of 11 844 earthquakes during February 2019 and August 2020 that are detected and archived by the Sichuan Earthquake Administration (SEA). These earthquakes were recorded by totally 29 permanent stations in the local surface seismic network (ID: SC) equipped with short-period seismometers at a sampling rate of 100 Hz. The direct *P* waveforms on the 29 stations are converted to frequency-domain observed spectra using a multitaper based method (MATLAB function: 'pmtm.m') as the input of the analysis. The time window of spectrum computation is the *P*–*S* arrival difference after the *P* arrival, covering the majority of the *P*-wave energy. We only use direct *P* waveforms in the analysis because the *S* waves usually couple with *P* wave or coda, potentially leading to biased frequency contents. Due to the limitation of instrument response, we exclude any frequency contents outside of 1–40 Hz range. To mitigate the influence

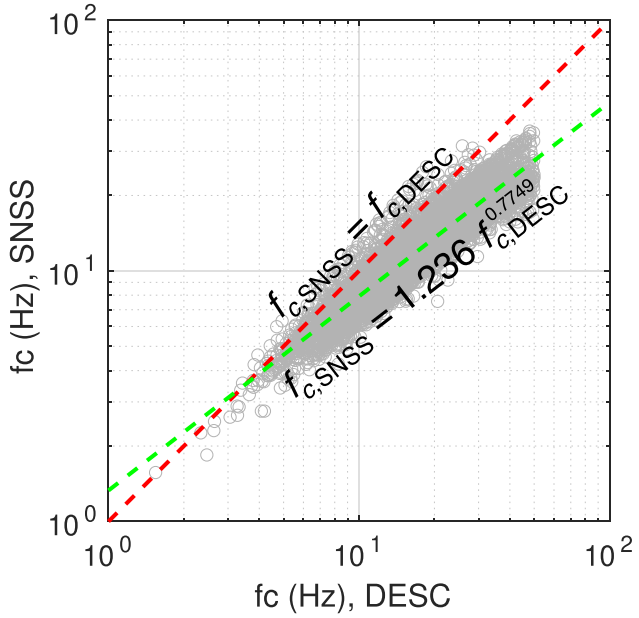

Figure 10. A one-to-one comparison of individual earthquake corner frequencies obtained using the DESC (*x*-axis) and SNSS (*y*-axis) methods (grey circles). The red dashed line indicates where the two methods share the same outputs, and the green dashed line describes the linear regression of the comparison on log10 scale.

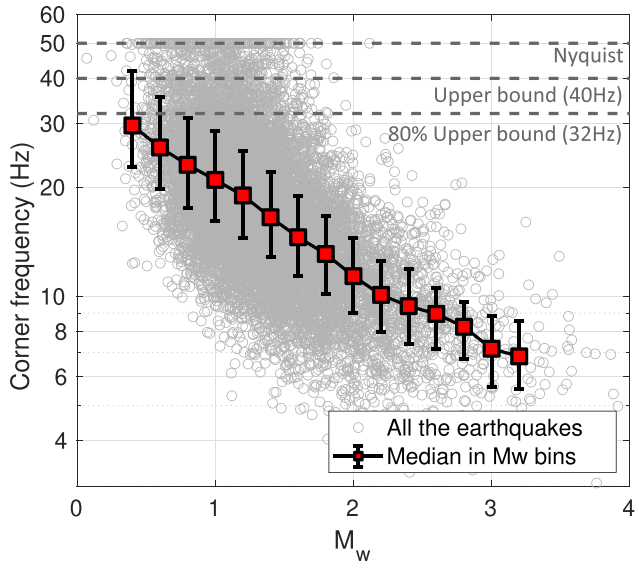

Figure 11. Corner frequency versus moment magnitude for all the earthquakes (grey circles). The red squares represent the median corner frequencies in different moment magnitude bins with an interval of 0.1 and a size of 0.1. The error bar represents the range of the corner frequencies between the first quartile and the third quartile in each magnitude bin. The horizontal dashed lines denote three corner frequency levels: at Nyquist (50 Hz), at the upper bound of the frequency band for spectral fitting (40 Hz) and at 80 per cent of the upper bound (32 Hz, the resolution limit as discussed in Chen & Abercrombie 2020), respectively.

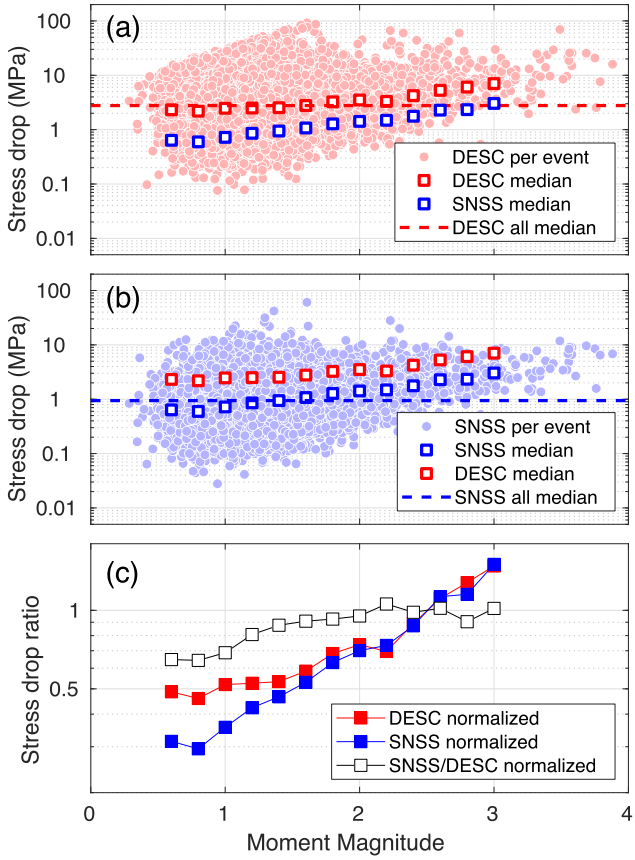

Figure 12. Magnitude dependence of stress drops in Rongxian area. (a and b) The stress drop magnitude dependence obtained using the DESC (a, red circles) and SNSS (b, blue circles) methods. The horizontal dashed lines are the median values of stress drops from each method, and the red and blue squares show the median values in magnitude bins with an increment of 0.2. The red and blue squares are the same in (a) and (b) for comparison between the two methods. (c) Normalized median values in (a) and (b) in the same magnitude bins by the median stress drops for $M_w > 2$ earthquakes (red and blue solid squares). The white squares indicate the ratios between the normalized stress drops in these magnitude bins as a comparison of the magnitude dependence from the two methods, which show that the stress drop differences between the two methods change with magnitude.

from noise, we apply strict criteria to screen out noisy waveforms: based on the noise spectrum calculated in the 1-s window before the *P* arrival, for each spectrum of an earthquake-station pair, 90 per cent of the frequency sampling points between 1 and 40 Hz shall have the SNR larger than 2, meanwhile 75 per cent of the frequency sampling points in the same frequency range shall have SNR larger than 3. The earthquakes above 1 km depth are not included as the earthquake energy in the sediment is attenuated differently than that at deeper depths. After the screening process, we obtain 94 744 reliable *P*-wave spectra that guarantee each earthquake among the 11 844 are recorded by at least four stations among the total 29. The local magnitudes of the earthquakes range from M_L 0–5.6 with a median of 1.3 according to the local earthquake catalogue produced by Sichuan Earthquake Administration, China. The moment magnitudes are important information required in the stress drop analysis; we use the published moment magnitudes in Yi *et al.* (2020) for the $M_L > 4$ earthquakes, but the smaller earthquakes do not hold moment magnitude records in the current catalogue. To obtain the moment magnitudes of these earthquakes, we follow the

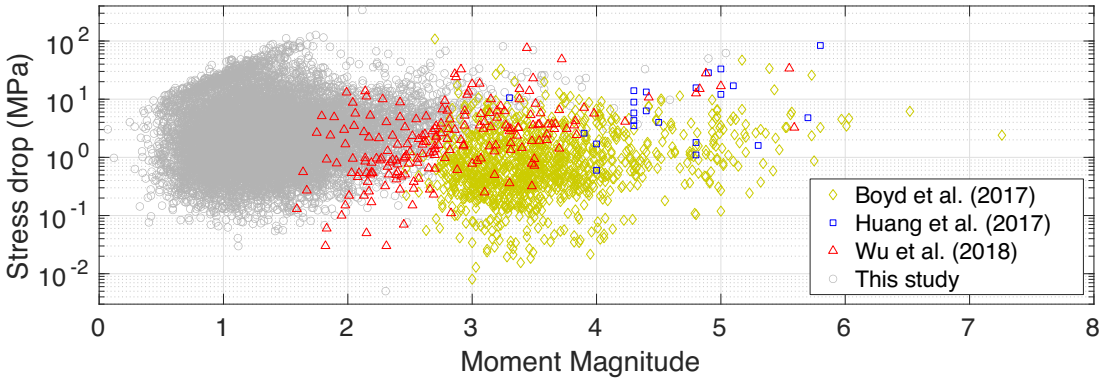

Figure 13. An overall comparison of stress drop magnitude dependence among four different studies as mentioned in the figure legend in different colours and markers.

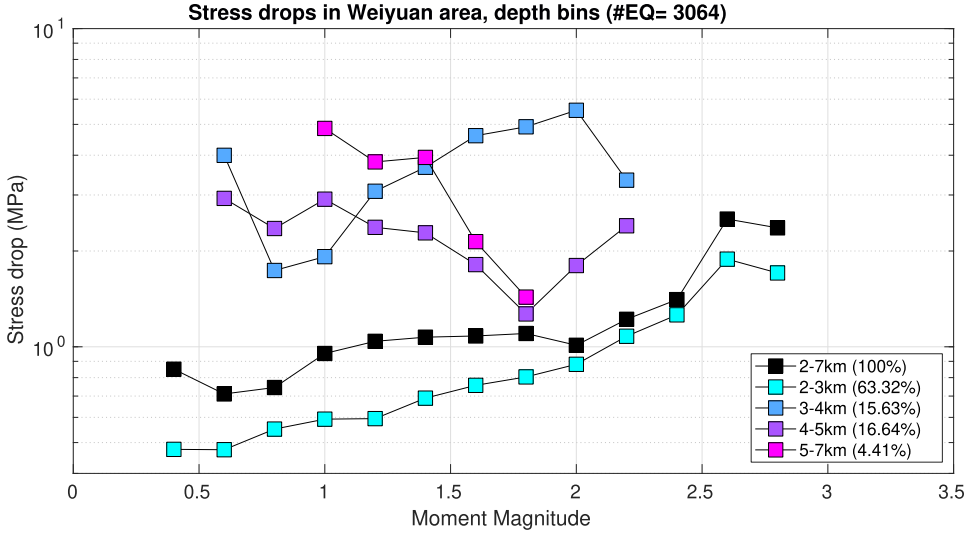

Figure 14. Stress drop magnitude dependence in different depth bins in the Weiyuan area. The percentage in the brackets in the figure legend indicates the number of earthquakes in each depth bin among all. The curves show the median value changes over magnitude with an increment of 0.2.

workflow in Zhang *et al.* (2022) to perform magnitude calibration and establish a conversion relationship from local magnitude to moment magnitude utilizing the 0.6–1.0 Hz average amplitude in the low-frequency plateau of the event spectra.

In this analysis, we carefully consider the data organization and parameter selection to mitigate the influence on the accuracy of the stress drops from different aspects. To correct for the attenuation heterogeneity of the underground medium mentioned in Section 2.1, we find 500 random base earthquakes in the data set across the whole studied area, and for each base earthquake, we select a set of 500 closest earthquakes to it as a subset of the data set and perform the DESC method within this base earthquake set, similar to the practice by Allmann & Shearer (2007). A certain earthquake may be included in multiple base event subsets, and we use the median stress drop of all its measurements from different subsets as its representative. In each subset, to describe the compactness of the earthquakes (aka. consistent attenuation in the area) we define the horizontal range as the square root of the summation of the distance between the 10th and the 90th quantiles of the longitudes and latitudes in km, respectively, and the depth range as the distance between the 10th and the 90th quantiles of the depths. For the 500 subsets, we find there are approximately 83 per cent of them hold horizontal ranges lower than 10 km, and 97 per cent hold depth ranges lower than 1 km, and both the ranges are tested valid that ensure consistent attenuation in the area (Zhang *et al.* 2022). This guarantees that the ECS for event spectra correction is spatially varying and accounts for the local attenuation level across different subsets, and the DESC method is applied in a compact area spanned by each subset so the assumption in Step 4 is valid. The magnitude bin size in the DESC workflow is set to 0.2. After obtaining an ECS in each base earthquake set, we fit the ECS-corrected source spectra to Brune-shape spectra and solve for the corner frequency within 1–40 Hz range. It is important to use higher upper bound in spectral fitting, because a narrower frequency band could result in underestimation of corner frequencies. Chen & Abercrombie (2020) performed a synthetic test revealing that the SNSS-similar approaches can recover the largest corner frequencies within approximately 80 per cent of the frequency upper bound before systematic underestimation happens. This implies that for a maximum of 40 Hz upper bound, an unbiased corner frequency cannot exceed around 32 Hz. Considering this factor, the magnitude range we use in the DESC workflow is set to at least M_w 0.9, and at most M_w 3.0 to avoid large-magnitude bins that contain too few earthquakes.

Following the setup of analysis discussed above, we perform the source parameter inversion for the 11 844 earthquakes in the whole

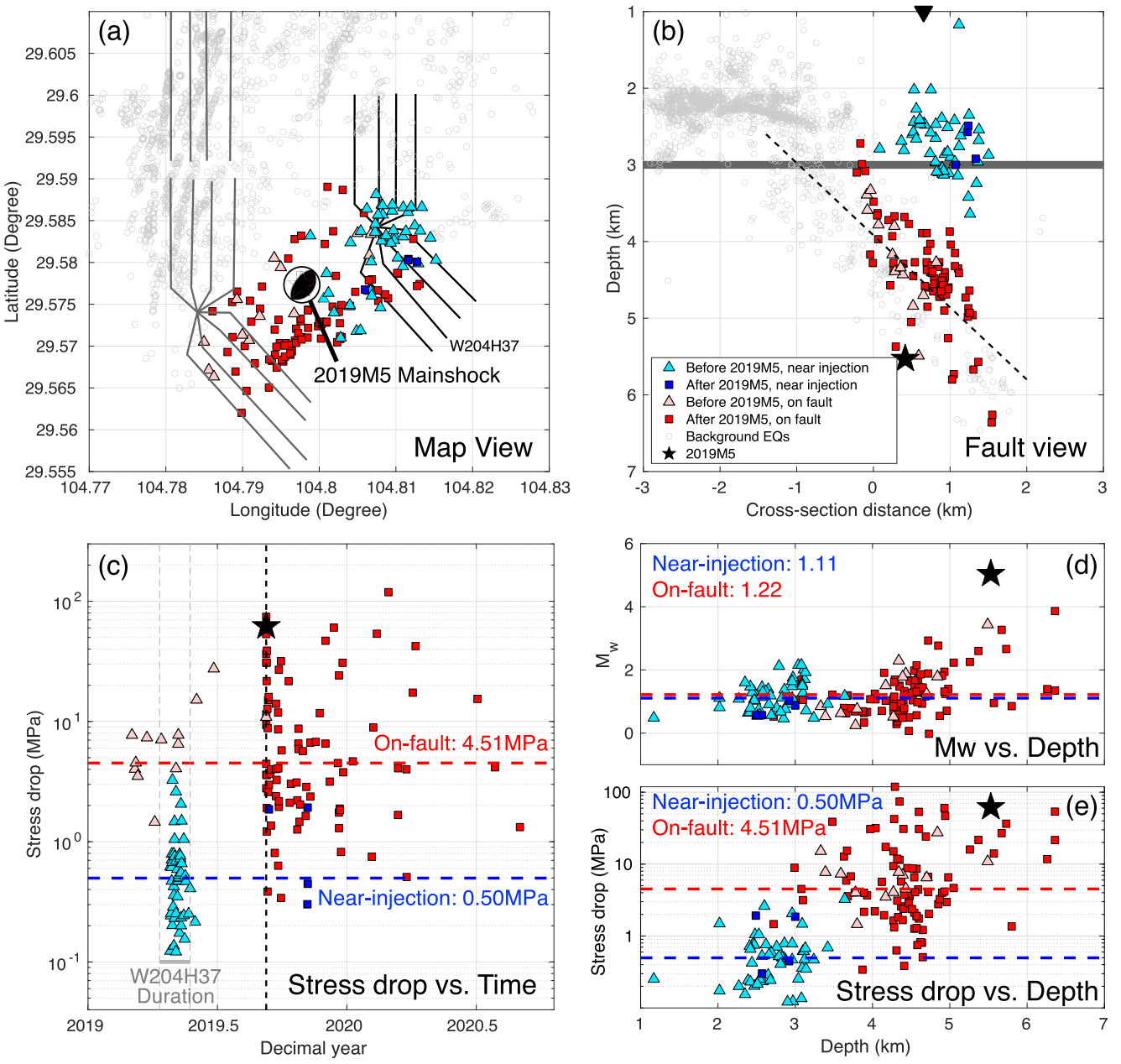

Figure 15. A zoom-in statistics figure near the September 2019 M_L 5 Weiyuan main shock. (a) A map view of the seismicity in the Sep 2019 M_L5 vicinity. The rectangles and squares represent the 152 earthquakes before and after the main shock in the time range from early-2019 to mid-2020, coloured by their locations (cyan and blue: before and after the main shock near the injection well, pink and red: before and after the main shock on the unmapped fault). The grey open circles show the background seismicity in this area in the whole data set. The beach ball pinpoints the main shock and describes its focal mechanism. The black traces mark the injection well W204H37 associated with the seismicity near it (cyan and blue markers), and the grey traces are nearby injection wells that could be coupled with some of the background injection-related seismicity. (b) A along-strike cross-section view of the same seismicity in (a). The grey thick line at 3 km depth marks the approximate fracturing depth of W204H37 well. The black dashed line is a delineation of the unmapped pre-existing fault where the main shock occurred. The black star marks the location of the main shock. The black reversed triangle is the surface location of the W204H37 well. (c) Temporal variation of the stress drops with the same marker and colouring schemes as those in (a) and (b). The horizontal solid lines show the median values of the two groups of earthquakes (blue: near-injection earthquakes, including the cyan and blue markers; red: on-fault earthquakes, including the pink and red markers). The interval framed by the vertical dashed grey lines and a horizontal solid grey line indicates the W204H37 well operation period. (d and e) Depth variation of the moment magnitudes (d) and stress drops (e) of the 152 earthquakes using the same marker and colouring schemes as previous. The horizontal dash lines mark the median moment magnitudes and median stress drops in the two groups, similar to those in (c).

RWZ area (geometry setup in Fig. 6a, and latitude-depth distribution in Fig. 6b). The maximum and minimum moment magnitudes are measured as 5.04 and −0.02, respectively, with a median of 1.30. The two magnitude scales generally follow the linear regression (Fig. 7):

$$M_w = 0.8826M_L + 0.1702 \quad (4)$$

This is found steeper than observed in Yi *et al.* (2020) using large earthquakes.

Next, we estimate the earthquake stress drops based on the obtained moment magnitudes and their event spectra (see spectra examples in Fig. 6c). The stress drops range from 0.14 to 41.94 MPa marked by the 1st and 99th percentile, which does not include some biased extremes outside this range due to limited corner frequency resolution. The median and geometric mean of stress drops are 2.29 and 2.32 MPa, respectively; the logarithmic standard deviation, describing the scattering of stress drops usually observed spanning a range of 3 orders of magnitude, is estimated to be 0.50 after excluding the earthquakes with outlier stress drop values. It should be mentioned that among these earthquakes, approximately 3.4 per cent are found to have unresolvable corner frequencies exceeding the upper limit of the instrument, meaning their stress drops should be biased; we manually set their corner frequencies to the Nyquist frequency (50 Hz) following the practice of Allman & Shearer (2007) and Zhang *et al.* (2022). Fig. 8(a) shows the strong heterogeneity of stress drops across the studied area. In Fig. 8(b), the red curve showing the fitting of log10 stress drop histogram to Gaussian distribution indicates the estimated stress drops are nearly normally distributed. Considering the heterogeneous nature of tectonic environments across the RWZ area, we separate the whole studied area into three roughly designed rectangular subareas (Fig. 8a): I. Rongxian Area (red rectangle), II. Weiyuan Area (green rectangle) and III. Zigong Area (blue rectangle).

I. The earthquakes in Rongxian area span a magnitude range of M_w 0.28–4.59, of which five earthquakes have M_w larger 4. Totally 99.0 per cent of the earthquakes are located shallower than 5 km depth. The median of the stress drops is 2.77 MPa, slightly higher than the overall stress drop median of the whole RWZ area. Higher stress drops are found in the injection area on the east of Molin Fault. In this area, multiple injection wells were being operated in the studied time range, including one well near the February 2019 M_L 4.9 main shock epicentre.

The stress drops in Rongxian area are found nearly independent to their depths after applying a depth-dependent rupture velocity model in the calculation (Figs 9 and A1). As for the moment magnitude, there is apparently weak dependence for earthquakes smaller than M_w 2, while those with $M_w > 2$ present visible dependence relationship (Figs 9 and B1). Higher stress drops are found near the September 2019 M_L 5 main shock, while the stress drops are found systematically lower to the north.

II. The magnitudes of the earthquakes in Weiyuan area range from M_w −0.02 to M_w 5.04, while there are more earthquakes found near and shallower than 2 km depth than those in Rongxian area (Figs 9 and B2). The median stress drop is estimated to be 1.06 MPa, around 61.7 per cent lower than that in Rongxian area, and 53.7 per cent lower than the overall median.

In Weiyuan area, the stress drops are observed significantly increasing in the depth range of 2–4 km, but their depth dependence disappears below 4 km (Figs 9 and A2). The observation here contradicts with a collection of studies in Abercrombie *et al.* (2021) showing almost non-depth-dependent patterns after applying the aforementioned spatial attenuation correction and shear wave velocity. Meanwhile, unlike that in Rongxian area, we find consistent magnitude dependence at lower and higher magnitudes. This is accompanied by 1.5 per cent of unresolvable corner frequencies, which should not cast large impact on the magnitude dependence.

III. Zigong area has the smallest population of earthquakes in the RWZ area (7.4 per cent of the total); meanwhile, they are narrowly distributed in terms of depth (around 3–6 km) and moment magnitude (mostly M_w 1.0–2.2; Figs 9, A3 and B3). Therefore, the stress drop statistics may be unreliable in this area. The median stress drop is the highest among all three areas (4.55 MPa), and it is unknown whether the difference in stress drops is due to the limited data.

5 DISCUSSIONS

5.1 DESC versus SNSS on Weiyuan shale gas field earthquakes

The synthetic tests in Section 3 have revealed that the DESC method outperforms the SNSS method in source parameter recovery; however, the complexity of the earthquake source processes and underground media, and the simple source model assumption make it unclear whether other factors could alter the test findings. To investigate whether the mitigation of source parameter estimation using the DESC method can be mapped to field data, we apply the SNSS method on the Weiyuan shale gas field data set and compare the results of corner frequencies and stress drops with those obtained above. We implement the same set of parameters on the SNSS trial, and the same data processing workflow to ensure no other factors bias the comparison.

We first compare the individual corner frequency estimates obtained using the two methods (Fig. 10). The corner frequencies from the SNSS method are systematically lower than those from the DESC method; the average corner frequency ratio between DESC and SNSS increase from about 1.1 at <5 Hz to 1.9 when the corner frequencies approach the upper bound of spectral fitting (40 Hz), which can be described with a log10 linear regression of $f_{c,SNSS} = 1.236\, f_{c,DESC}^{0.7749}$. The comparison of corner frequencies near the 40 Hz upper bound may be influenced by the limited frequency band, but such influence could be minimal because Fig. 11 shows that the median corner frequency of an M_w 1.5 earthquake should be approximately 15.39 Hz obtained using the DESC method, which is 38.5 per cent of the upper bound; Chen & Abercrombie (2020) discussed that when averaged from multiple stations, corner frequencies lower than 40–80 per cent of the frequency upper bound are more likely to be resolvable (i.e. within 25 per cent of true corner frequency), while higher corner frequencies tend to be systematically underestimated. The result in Fig. 10 indicates that the difference of the two methods enlarges with higher corner frequencies, which agrees with the discussion in Chen & Abercrombie (2020) and Zhang *et al.* (2022). Furthermore, a similar pattern was observed by Shearer *et al.* (2019) who found that the spectral ratio method results in larger corner frequency estimates than a previous stacking-based approach when the Brune's model is applied, and the difference is enlarged for earthquakes with higher corner frequencies (Fig. 8 in Shearer *et al.* 2019). This indicates that the DESC approach could produce similar source parameter estimates to those by the spectral ratio method, while the previous stacking-based approach could lead to systematic source parameter underestimation.

The enlarged corner frequency ratio between the DESC and SNSS methods at higher corner frequencies could suggest relatively larger stress drop underestimation for lower magnitude earthquakes. To visualize this, we compare the magnitude dependence of individual stress drops obtained using the two methods in the Rongxian area (Fig. 12). Based on the magnitude dependence measurements using the DESC method in Fig. 9, we observe extra magnitude scaling of the SNSS stress drops over the DESC stress drops (Fig. 12c): the ratio of the normalized median stress drops between the SNSS and

DESC ones increases with earthquake moment magnitude from M_w 0.6 to 2.0, and the excessive underestimation can be as high as 31.3 per cent at M_w 1.0; the discrepancy in magnitude scaling becomes ignorable for $M_w > 2.2$. The case with STD = 0.5, $k = 0.5$ and input_stress_drop = 3.3 MPa in the synthetic test shows approximately 10 per cent of excessive underestimation of the SNSS method at M_w 1.0, which is about 21.3 per cent lower than the realistic extent. This indicates that the stacking issue still inevitably affects the evaluation of earthquake self-similarity, albeit not the dominant factor.

Figs 12(a) and (b) shows that the absolute stress drops derived from both methods are remarkably different. We obtain an overall median stress drop of 0.94 MPa in the Rongxian area, while the DESC method as mentioned before outputs a median of 2.77 MPa in the same area, which is nearly three times of difference; more specifically, the difference varies at different magnitudes—there is a 71 and 60 per cent underestimation at M_w 1.0 and M_w 2.0, respectively from the SNSS method relevant to the DESC stress drops. As a comparison, the case in the synthetic test 3.2 with the closest setup is STD = 0.5, k = 0.5 and input_stress_drop = 3.3 MPa, and we obtain approximately 19 and 14 per cent underestimation at M_w 1.0 and M_w 2.0, respectively. Apparently, the extent of underestimation reflected from the tests are 52 and 46 per cent lower than the realistic underestimation at the two moment magnitudes.

The comparison of the two methods differs significantly between realistic data sets and synthetic data sets, which may infer that extra factors also cast influence on the realistic stress drop estimates. Since the two methods implement the same spectral fitting approach to obtain the individual corner frequencies for the earthquakes, the key leading to the discrepancy of synthetic data set stress drops from the two methods is the different ways the ECS is generated in the two methods. The magnified excessive underestimation from the SNSS method in the realistic data set could suggest that the corresponding ECS may have to correct further biased stacked spectra from other factors, such as the residual part of the event spectra produced in the spectral decomposition stage. The residual part cannot be directly quantified, therefore it is hard to realize its simulation in the synthetic tests. This factor should not strongly impact the DESC results, as it does not involve direct stacking of event spectra. Another possible factor is the source model assumption—though the circular crack model has been widely applied, due to the limitations in the observatory means it is uncertain how much difference there is between the popular model and the reality; it is hard to explain why Brune's model is more suitable than other empirical models for spectral fitting here as past studies have shown that Brune's and Boatwright's model (Boatwright 1980) result in different stress drop levels (Huang *et al.* 2016; Ruhl *et al.* 2017; Demuth *et al.* 2019; Shearer *et al.* 2019), though Chen & Abercrombie (2020) showed that Brune's model with a smoother corner is more suitable for averaged source spectra, which does not apply to the DESC method case; therefore it is unpredictable whether the significant difference of magnitude dependence in the synthetic and realistic data set is caused by the source model assumptions. Provided these, it is still persuasive that the stress drop measurements from the proposed method are less underestimated compared to before.

5.2 Stress drop characteristics and earthquake triggering mechanisms

Our stress drop estimates of induced earthquakes in the whole Weiyuan shale gas field area generally fall into a similar range to that of the induced earthquakes in Oklahoma (Wu *et al.* 2018; Fig. 13, red). The median stress drops of the two different area are 2.29 and 2.07 MPa, and both studies find significant spatial variability across their corresponding studied area. Both studies also report larger stress drops for $M_w > 2$–2.5 earthquakes than smaller ones below M_w 2–2.5 on average. Unlike the induced earthquakes in Oklahoma, the overall USA crustal earthquakes show relatively lower median stress drops (approximately 0.71 MPa) than those of our induced earthquakes (Boyd *et al.* 2017; Fig. 13, yellow). This can possibly be ascribed to the limited capability of resolving low-magnitude earthquake corner frequencies, or the variety of focal mechanisms across the Northern America continent. Boyd *et al.* (2017) reported low stress drops of Central USA with majorly normal to strike-slip faults, intermediate stress drops of Western USA with a mixture of multiple mechanisms, and high stress drops of Eastern USA which is thrust-fault-dominant. As the Weiyuan shale-gas field is thrust-dominant as shown by Yi *et al.* (2020), our stress drops on average (2.32 MPa) should be seen as comparable to the estimates in Eastern USA in Boyd *et al.* (2017) (approximately 2.99 MPa) due to the similar source mechanisms. The stress drop variability across mechanisms is further confirmed by Huang *et al.* (2017) (Fig. 13, blue). The reported stress drops are overall higher than any of the list studies, but these are relatively larger earthquakes and have similar stress drop estimates as the large earthquakes in Wu *et al.* (2018) and our results. It should be noted that the relationship between stress drops and focal mechanisms are challenged by Allmann & Shearer (2009) and Oth (2013) who found strike-slip-dominant areas tend to yield higher stress drops than thrust-dominant areas, and one cannot either ignore the discrepancies of parameters used among studies, for example rupture velocity assumption; however, the comparison among different studies still show the stress drops across tectonic environment, focal mechanisms and different methods do not systematically differ.

The stress drop consistency among studies does not explain why the stress drop estimates change 7–10 times over depth in Weiyuan region (Figs 9 and A2). We break the Weiyuan area earthquakes into different depth bins: 2–3 km, 3–4 km, 4–5 km and 5–7 km (Fig. 14), and observe a large gap of stress drops at 3 km in terms of both the absolute values and magnitude dependence. The Weiyuan area is dominated by earthquakes shallower than 3 km (over 60 per cent). At the depth range of 2–3 km, the stress drops are found scaling with moment magnitudes significantly between M_w 0.4 and M_w 2.8, with higher-magnitude earthquakes (near M_w 3) having comparable stress drops to deeper earthquakes, and lower-magnitude earthquakes holding obviously lower values. For earthquakes deeper than 3 km, the magnitude dependence of stress drops is nearly non-existent overall across the entire magnitude range. This could suggest that the 3 km depth could be a boundary of different earthquake triggering processes. It is reasonable to suspect that shallower earthquakes are more directly engaged with fracturing activities provided the active operations at 3–3.5 km depth in this area (Ma *et al.* 2020) during the studied time periods, as Goertz-Allmann *et al*. (2011) and Igonin *et al.* (2023) reported that the stress drops of seismicity near injection spots are lower than the ambient ones coupled with pre-existing faults.

We zoom into 152 earthquakes near the September 2019 M 5 earthquake in the Weiyuan area from early 2019 to mid 2020, during which an injection well W204H37 is under operation near the hypocentre of the M 5 earthquake (Fig. 15a). Fig. 15 shows two groups of earthquakes: (1) the shallow earthquakes occurred mainly 3–4 months before the M 5 main shock coinciding with the W204H37 operation time, thus are more injection-coupled; (2) the deeper earthquakes on the unmapped fault that hosted the M 5 main

shock and most on-fault earthquakes occurred after the main shock, thus more main shock-coupled. There are also minor earthquakes occurred before the main shock on the fault, and after the main shock near the injection (Figs 15b and c). The median stress drop of the injection-coupled earthquakes and main shock-coupled earthquakes are about 0.50 and 4.51 MPa, denoting an approximately 9.02 times of difference generally agreeing with that in Figs 9 and A2. Fig. 15(b) show that the two groups of earthquakes are dominant in the depth ranges of above-3.5 km and below-3.5 km, respectively; the difference of stress drop level in the two depth ranges is unlikely due to natural depth dependence, as we do not observe significant depth variation of stress drops below 3 km in Weiyuan area (Figs 9, A2 and 15d, (1)), or across the whole depth range in Rongxian area. Magnitude dependence may also unlikely cause the difference, as we find barely different moment magnitudes in the two groups (medians of 1.11 and 1.22, respectively); if we ascribe the large discrepancy in stress drop level to magnitude dependence in the area, then according to Fig. 9(B2), the median stress drops at M_w 1.11 and M_w 1.22 are 2.30 and 2.12 MPa resulting in a difference of only 0.92 times, which cannot account for the $9.02/0.92 = 9.80$ times of difference. The different stress drops between the two groups could instead originate from the discrepancy in pore pressure conditions near and far from the injection well (Zoback 2010; Goertz-Allmann *et al*. 2011). The pore pressure near the injection well can be as high as nearly 100 MPa in this area (Yi *et al.* 2020), while the silence of seismicity in time and space between the W204H37 operation zone and the 2019 M 5 aftershocks may be a result of lacking fluid migration channel from the injection zone above 3 km into the pre-existing fault, or the fault being not as critical to be activated by possible fluid migration (Yu *et al.* 2020). Therefore, it is plausible to conclude that different triggering mechanisms (direct injection-induced earthquakes VS. possible aftershocks) could have different stress drops, though unfortunately further analysis is limited by confidential injection data that is not available for public access. It should also be noted that no assertions can be made that the different stress drops in the two groups are unrelated to natural depth dependence and magnitude dependence of stress drops, because we do not observe similar temporal and special separation in other subareas. We expect to answer the question above in the future with the help of a latest dense array deployed in the studied region.

6 CONCLUSIONS

We propose a new method that improves the earthquake stress drop workflow, and apply the method to solving for the induced earthquake source parameters in the Weiyuan Shale Gas Field in Sichuan, China. It is observed that:

1. The proposed method based on global optimization is capable of mitigating the source parameter underestimation compared to traditional methods relying on stacking of earthquake source spectra.
2. The stress drops show strong heterogeneity over space in the studied region, and are found nearly self-similar at low magnitudes and non-self-similar at high magnitudes. The stress drops are depth-dependent in the Weiyuan area rather than in the Rongxian area.
3. The overall stress drop level in Weiyuan Shale Gas Field exhibits no systematic difference than that in other tectonic environment; However, stress drop discrepancy is still found for possibly different underlying mechanisms associated with different pore pressure levels.

SUPPORTING INFORMATION

Supplementary data are available at *GJI* online.

Figure S1. Left-hand panel: statistics of the DESC stress drop convergence in different magnitude bins in five different trials with the same data set. Trials are differentiated using different colours. Right: A comparison of the time complexity (in seconds) of the DESC and SNSS methods. Blue curve shows the runtimes of 20 trials using the SNSS method, the red solid curve shows the runtimes of 20 trials of the DESC method allowing 500 iterations, and the red dashed curve shows the runtimes of 20 trials using the DESC method stopped after 260 iterations where the convergence becomes relatively stable.

Figure S2. A full version of Fig. 5 showing the results of all the test cases with the same markers.

Please note: Oxford University Press is not responsible for the content or functionality of any supporting materials supplied by the authors. Any queries (other than missing material) should be directed to the corresponding author for the paper.

ACKNOWLEDGMENTS

We are grateful to Drs Xinglin Lei, Yajing Liu, Junlun Li and Risheng Chu for their comments on framing this work, and inspiring discussions to improve the logic and workflow. We also appreciate the effort and time of Dr Jean-Philippe Avouac and an anonymous reviewer on carefully reviewing the manuscript, as well as their valuable comments that push the work towards completion. This work is under the support of the National Natural Science Foundation of China (No. U2139203), Hong Kong Research Grant Council (No. 14303721), Faculty of Science in The Chinese University of Hong Kong. The earthquake beach balls are plotted using MATLAB package 'focalmech' (https://www.mathworks.com/matlabcentral/fileexchange/61227-focalmech-fm-centerx-centery-diam-varargin).

DATA AVAILABILITY

The waveform data is provided by The Sichuan Earthquake Administration upon request.

AUTHOR CONTRIBUTION

Conceptualization: JZ, HY; Data Curation: JS; Investigation: HY, JZ, XC; Methodology: JZ; Supervision: HY; Visualization: JZ; Writing-original draft: JZ; Writing-review and editing: JZ, HY, JZ, XC; Project Administration: HY. Funding Acquisition: HY.

REFERENCES

Abercrombie, R.E., 2014. Stress drops of repeating earthquakes on the San Andreas Fault at Parkfield, *Geophys. Res. Lett.,* **41,** 8784–8791.

Abercrombie, R.E. *et al.* 2021. Does earthquake stress drop increase with depth in the crust?, *J. geophys. Res.,* **126,** 1–22.

Agurto-Detzel, H., Bianchi, M., Prieto, G.A. & Assumpção, M., 2017. Earthquake source properties of a shallow induced seismic sequence in SE Brazil, *J. geophys. Res.,* **122,** 2784–2797.

Allmann, B.P. & Shearer, P.M., 2007. Spatial and temporal stress drop variations in small earthquakes near Parkfield, California, *J. geophys. Res.,* **112,** 1–17.

Allmann, B.P. & Shearer, P.M., 2009. Global variations of stress drop for moderate to large earthquakes, *J. geophys. Res.,* **114,** 1–22.

Baltay, A.S., Hanks, T.C. & Abrahamson, N.A., 2019. Earthquake stress drop and Arias intensity, *J. geophys. Res.,* **124,** 3838–3852.

Bindi, D., Spallarossa, D., Picozzi, M. & Morasca, P., 2020. Reliability of source parameters for small events in central Italy: insights from spectral decomposition analysis applied to both synthetic and real data, *Bull. seism. Soc. Am.,* **110,** 3139–3157.

Boatwright, J., 1980. A spectral theory for circular seismic sources; simple estimates of source dimension, dynamic stress drop, and radiated seismic energy, *Bull. seism. Soc. Am.,* **70,** 1–27.

Boyd, O.S., McNamara, D.E., Hartzell, S. & Choy, G., 2017. Influence of lithostatic stress on earthquake stress drops in North America, *Bull. seism. Soc. Am.,* **107,** 856–868.

Brune, J.N., 1970. Tectonic stress and the spectra of seismic shear waves from earthquakes, *J. geophys. Res.,* **75,** 4997–5009.

Chen, X. & Abercrombie, R.E., 2020. Improved approach for stress drop estimation and its application to an induced earthquake sequence in Oklahoma, *Geophys. J. Int.,* **223,** 233–253.

Chen, X. & Shearer, P.M., 2013. California foreshock sequences suggest aseismic triggering process, *Geophys. Res. Lett.,* **40,** 2602–2607.

Chu, R. & Sheng, M., 2023. Stress features inferred from induced earthquakes in the Weiyuan Shale gas block in Southwestern China, *J. geophys. Res.,* **128,** 1–14.

Demuth, A., Tjåland, N. & Ottemöller, L., 2019. Earthquake source parameters in Norway determined with empirical Green's functions, *J. Seismol.,* **23,** 715–724.

Eshelby, J.D., 1957. The determination of the elastic field of an ellipsoidal inclusion, and related problems, *Proc. R. Soc. Lond., A,* **241,** 376–396.

Gharti, H.N., Oye, V., Roth, M. & Kuhn, D., 2010. Automated microearthquake location using envelope stacking and robust global optimization, *Geophysics,* **75**(4), doi:10.1190/1.3432784.

Goebel, T.H.W., Hauksson, E., Shearer, P.M. & Ampuero, J.P., 2015. Stress-drop heterogeneity within tectonically complex regions: a case study of San Gorgonio Pass, southern California, *Geophys. J. Int.,* **202,** 514–528.

Goertz-Allmann, B.P., Goertz, A. & Wiemer, S., 2011. Stress drop variations of induced earthquakes at the Basel geothermal site, *Geophys. Res. Lett.,* **38**(9), doi:10.1029/2011GL047498.

Holmgren, J.M., Atkinson, G.M. & Ghofrani, H., 2019. Stress drops and directivity of induced earthquakes in the western Canada sedimentary basin, *Bull. seism. Soc. Am.,* **109,** 1635–1652.

Huang, Y., Beroza, G.C. & Ellsworth, W.L., 2016. Stress drop estimates of potentially induced earthquakes in the Guy-Greenbrier sequence, *J. geophys. Res.,* **121**(9), 6597–6607.

Huang, Y., Ellsworth, W.L. & Beroza, G.C., 2017. Stress drops of induced and tectonic earthquakes in the central United States are indistinguishable, *Sci. Adv.,* **3,** 1–8.

Igonin, N., Trugman, D.T., Gonzalez, K. & Eaton, D.W., 2023. Spectral characteristics of hydraulic fracturing-induced seismicity can distinguish between activation of faults and fractures, *Seismol. Res. Lett.,* **94**(4), 1791–1806.

Kaneko, Y. & Shearer, P.M., 2014. Seismic source spectra and estimated stress drop derived from cohesive-zone models of circular subshear rupture, *Geophys. J. Int.,* **197,** 1002–1015.

Kaneko, Y. & Shearer, P.M., 2015. Variability of seismic source spectra, estimated stress drop, and radiated energy, derived from cohesive-zone models of symmetrical and asymmetrical circular and elliptical ruptures, *J. geophys. Res.,* **120,** 1053–1079.

Klinger, A.G. & Werner, M.J., 2022. Stress drops of hydraulic fracturing induced microseismicity in the Horn River basin: challenges at high frequencies recorded by borehole geophones, *Geophys. J. Int.,* **228,** 2018–2037.

Lengliné, O., Lamourette, L., Vivin, L., Cuenot, N. & Schmittbuhl, J., 2014. Fluid-induced earthquakes with variable stress drop, *J. geophys. Res.,* **119,** 8900–8913.

Ma, X. *et al.* 2020. Dominating factors on well productivity and development strategies optimization in Weiyuan shale gas play, Sichuan Basin, SW China, *Shiyou Kantan Yu Kaifa/Petroleum Explor. Dev.,* **47,** 555–563.

Madariaga, R., 1976. Dynamics of an expanding circular fault, *Bull. seism. Soc. Am.,* **66,** 639–666.

Mayeda, K., Gök, R., Walter, W.R. & Hofstetter, A., 2005. Evidence for non-constant energy/moment scaling from coda-derived source spectra, *Geophys. Res. Lett.,* **32,** 1–4.

Oth, A., 2013. On the characteristics of earthquake stress release variations in Japan, *Earth planet. Sci. Lett.,* **377-378,** 132–141.

Oth, A., Bindi, D., Parolai, S. & di Giacomo, D., 2011. Spectral analysis of K-NET and KiK-net data in Japan, part II: on attenuation characteristics, source spectra, and site response of borehole and surface stations, *Bull. seism. Soc. Am.,* **101,** 667–687.

Oye, V., Bungum, H. & Roth, M., 2005. Source parameters and scaling relations for mining-related seismicity within the Pyhäsalmi ore mine, Finland, *Bull. seism. Soc. Am.,* **95,** 1011–1026.

Pennington, C.N., Chen, X., Abercrombie, R.E. & Wu, Q., 2021. Cross validation of stress drop estimates and interpretations for the 2011 Prague, OK, earthquake sequence using multiple methods, *J. geophys. Res.,* **126,** 1–24.

Ruhl, C.J., Abercrombie, R.E. & Smith, K.D., 2017. Spatiotemporal variation of stress drop during the 2008 Mogul, Nevada, earthquake swarm, *J. geophys. Res.,* **122,** 8163–8180.

Shearer, P.M., Abercrombie, R.E. & Trugman, D.T., 2022. Improved stress drop estimates for M 1.5 to 4 earthquakes in Southern California from 1996 to 2019, *J. geophys. Res.,* **127,** 1–23.

Shearer, P.M., Abercrombie, R.E., Trugman, D.T. & Wang, W., 2019. Comparing EGF methods for estimating corner frequency and stress drop from P wave spectra, *J. geophys. Res.,* **124**(4), 3966–3986.

Shearer, P.M., Prieto, G.A. & Hauksson, E., 2006. Comprehensive analysis of earthquake source spectra in southern California, *J. geophys. Res.,* **111,** 1–21.

Storn, R. & Price, K., 1997. Differential evolution—a simple and efficient heuristic for global optimization over continuous spaces, *J. Glob. Optim.,* **11,** 341–359.

Trugman, D.T. & Shearer, P.M., 2017. Application of an improved spectral decomposition method to examine earthquake source scaling in Southern California, *J. geophys. Res.,* **122,** 2890–2910.

Uchide, T., Shearer, P.M. & Imanishi, K., 2014. Stress drop variations among small earthquakes before the 2011 Tohoku-oki, Japan, earthquake and implications for the main shock, *J. geophys. Res.,* **119,** 7164–7174.

Wu, Q., Chapman, M. & Chen, X., 2018. Stress-drop variations of induced earthquakes in Oklahoma, *Bull. seism. Soc. Am.,* **108,** 1107–1123.

Wu, X. *et al.* 2019. Water availability assessment of shale gas production in the Weiyuan play, China, *Sustainability,* **11**(3), doi:10.3390/su11030940.

Yang, H., Zhou, P., Fang, N., Zhu, G., Xu, W., Su, J., Meng, F. & Chu, R., 2020. A shallow shock: the 25 February 2019 ML 4.9 earthquake in the Weiyuan Shale Gas Field in Sichuan, China, *Seismol. Res. Lett.,* **91,** 3182–3194.

Yi, G., Long, F., Liang, M., Zhao, M. & Wang, S., 2020. Geometry and tectonic deformation of seismogenic structures in the Rongxian-Weiyuan-Zizhong region, Sichuan Basin: insights from focal mechanism solutions. *Chinese J. Geophys. (in Chinese),* **63**(9), 3275–3291.

Yu, H., Harrington, R.M., Kao, H., Liu, Y., Abercrombie, R.E. & Wang, B., 2020. Well proximity governing stress drop variation and seismic attenuation associated with hydraulic fracturing induced earthquakes, *J. geophys. Res.,* **125,** 1–17.

Zeng, Q., Chu, R., Sheng, M. & Wei, Z., 2020. Seismic ambient noise tomography for shallow velocity structures beneath Weiyuan, Sichuan, *Chinese J. Geophys. (in Chinese),* **63**(3), 944–955.

Zhang, J., Chen, X. & Abercrombie, R.E., 2022. Spatiotemporal variability of earthquake source parameters at Parkfield, California, and their relationship with the 2004 M6 earthquake, *J. geophys. Res.,* **127,** 1–22.

Zhang, J., Zhang, H., Zhang, Y. & Liu, Q., 2016. Calibrating one-dimensional velocity model for downhole microseismic monitoring using station-pair differential arrival times based on the differential evolution method, *Phys. Earth planet. Inter.,* **261,** 124–132.

Zi, J., Yang, H., Su, J. & Chen, L., 2023. Structural constraints of induced earthquakes in the Weiyuan Shale Gas Field revealed by high-resolution body-wave tomography and earthquake relocation, *Tectonophysics,* **864,** doi:10.1016/j.tecto.2023.230007.

Zoback, M.D., 2010. *Reservoir Geomechanics*. Cambridge Univ. Press.

APPENDIX: MATHEMATICS BEHIND THE SYNTHETIC TESTS

It has been shown in Section 3.1 that a stacked spectrum from Brune-shape spectra is distorted and deviates from Brune shape causing biased source parameter estimation. This can be further proved from the aspect of mathematics. The biases include the underestimation of absolute values, the increased underestimation for lower magnitudes, and the higher underestimation with increased stress drop standard deviation (meaning the spectra used for stacking less resemble each other).

We consider a base case, where there are only two earthquakes for spectral stacking. The conclusion can be easily extended to complex cases with multiple earthquakes. The two earthquakes have similar magnitudes M_{w1} and M_{w2}, and their corner frequencies are f_{c1} and f_{c2}, respectively. The stacked spectrum of the two is compared with a reference spectrum with a moment of M_w and a corner frequency of f_c. The relationship between the two spectra and the reference spectrum follows below:

$$\begin{cases} M_w = (M_{w1} + M_{w2})/2, \\ f_c = \sqrt{f_{c1} f_{c2}}, \quad f_{c1} = k f_c, \quad f_{c2} = (1/k) f_c, \quad k > 1. \end{cases} \tag{A1}$$

The second equation of eq. (A1) means the corner frequencies (also stress drops) of the two earthquakes are geometrically symmetric to the reference corner frequency and follow Gaussian distribution. The log10 spectra of the two earthquakes $S_1(f)$ and $S_2(f)$ and the reference spectrum $S_0(f)$ in log10 scale can be expressed below:

$$\begin{cases} S_1(f) = C_1 - \log_{10}\left(1 + (f/f_{c1})^2\right) \\ S_2(f) = C_2 - \log_{10}\left(1 + (f/f_{c2})^2\right) \\ S_0(f) = C_0 - \log_{10}\left(1 + (f/f_c)^2\right), \end{cases} \tag{A2}$$

where f represents frequency samples, and $C_{0,1,2}$ represent the low frequency amplitudes of the log10 spectra, which are proportional the log10 moments corresponding to the two earthquakes and the reference. Therefore, we have $C_0 = C_1 + C_2$. The stacked spectrum of the two earthquakes $S(f)$ can be represented as:

$$S(f) = (S_1(f) + S_2(f))/2 = C_0 - \log_{10}\sqrt{\left(1 + (f/kf_c)^2\right)\left(1 + (kf/f_c)^2\right)}, \tag{A3}$$

$S(f)$ is compared to Brune spectrum to estimate a corner frequency f_{ci} standing for the inverted corner frequency of the stacked spectrum, which will be compared to f_c. We define m as the ratio, where:

$$m = f_{ci}/f_c \tag{A4}$$

The fitting of $S(f)$ to Brune shape is defined as $S_i(f)$:

$$S_i(f) = C_0 - \log_{10}\left(1 + (f/f_{ci})^2\right) = C_0 - \log_{10}\left(1 + (f/mf_c)^2\right). \tag{A5}$$

We shall prove that:

(1) $\boldsymbol{m < 1}$, meaning the corner frequency is underestimated.
(2) $\boldsymbol{m}$ **decreases with** $\boldsymbol{k}$, meaning the underestimation is larger when the scattering of stress drops becomes more significant.
(3) $\boldsymbol{m}$ **decreases with** $\boldsymbol{f_c}$, meaning the corner frequency of a smaller earthquake is more significantly underestimated than a larger earthquake.

1 Proof of underestimation

Comparing $S(f)$ and $S_i(f)$, we obtain:

$$S(f) - S_i(f) = 0.5 \log_{10} \frac{\left(1 + \left(\frac{f}{mf_c}\right)^2\right)}{\left(1 + \left(\frac{f}{kf_c}\right)^2\right)\left(1 + \left(\frac{kf}{f_c}\right)^2\right)} =: 0.5 \log_{10} R(f) \tag{A6}$$

$S(f)$–$S_i(f)$ has the same monotonicity as $R(f)$, to obtain the extreme value of the former we just need to compare the numerator and the denominator of $R(f)$, which we define as $D(f)$:

$$D(f) = \left(1 + (f/mf_c)^2\right)^2 - \left(1 + (f/kf_c)^2\right)\left(1 + (kf/f_c)^2\right) = \left(\frac{2}{m^2} - k^2 - \frac{1}{k^2}\right)(f/f_c)^2 + \left(\frac{1}{m^4} - 1\right)(f/f_c)^4 \tag{A7}$$

$D(f)$ should be zero; if the coefficient of the two terms in $D(f)$ are non-zero, let $p = m^2$, we obtain:

$$(f/f_c)^2 = \frac{\left(k^2 + \frac{1}{k^2}\right)p^2 - 2p}{1 - p^2} > 0. \tag{A8}$$

From the equation above, we have:

$$\frac{2}{k^2 + 1/k^2} < p < 1, \quad \sqrt{\frac{2}{k^2 + 1/k^2}} < m < 1. \tag{A9}$$

This indicates that as long as the two earthquakes have different corner frequencies, the inverted corner frequency of the stacked spectrum is always underestimated.

There is another case where $D(f)$ has two zero coefficients in eq. (A7):

$$\begin{cases} \frac{2}{p} - k^2 - \frac{1}{k^2} = 0 \\ 1 - p^2 = 0 \end{cases} \Rightarrow \begin{cases} p = 1,\ m = 1 \\ k = 1. \end{cases} \tag{A10}$$

This means the only situation where the underestimation does not happen is when the two earthquakes have the same corner frequency. Now we have proved that when the stress drops are scattered for the stacked earthquakes, the corner frequency of the stacked spectrum is always underestimated.

2 Proof of increased underestimation with stress drop scattering

Let $q = (f/f_c)^2$ which is constant when we only change the extent of scattering, we obtain:

$$q = \left(k^2 + \frac{1}{k^2}\right) p^2 - 2p, \quad m = \sqrt{p} = \sqrt{\frac{q}{\sqrt{1 + q\left(k^2 + \frac{1}{k^2} + q\right)} - q}}. \tag{A11}$$

In the equation above, since $k^2 + 1/k^2$ monotonically increases with k for $k > 1$, a larger k results in a smaller m. This proves that when the scattering of stress drops increases, the underestimation of the corner frequency of the stacked spectrum becomes larger.

3 Proof of larger corner frequency underestimation for smaller earthquakes

Smaller earthquakes on average have higher corner frequencies due to smaller fault dimensions. In eq. (A8), we can relate the reference corner frequency f_c to the ratio m. We define $A(p)$ and $B(p)$ as the numerator and denominator of $(f/f_c)^2$:

$$(f/f_c)^2 = \frac{\left(k^2 + \frac{1}{k^2}\right) p^2 - 2p}{1 - p^2} =: \frac{A(p)}{B(p)}. \tag{A12}$$

Now we inspect the monotonicity of $A(p)$ and $B(p)$ by calculating their derivatives to p. For $A(p)$, given eq. (A9) we have:

$$A'(p) = 2p\left(k^2 + \frac{1}{k^2}\right) - 2 > 2 > 0. \tag{A13}$$

This means $A(p)$ (the numerator) monotonically increases with p. For $B(p)$, we have:

$$B'(p) = -2p < 0. \tag{A14}$$

This means $B(p)$ (the denominator) monotonically decreases with p. Combining eqs (A13) and (A14), we can conclude that $(f/f_c)^2$ monotonically increases with p and m, thus m monotonically decreases with f_c. Now we have proved that there is outstanding underestimation for smaller earthquakes.

We have explained the intrinsic reason of the test results in Section 3.1 using mathematical derivation. In fact, the derivation above for two earthquakes can be applied to multiple earthquakes cases by grouping every two earthquakes according to their average magnitude.